HERON is jointly edited by:
STEVIN-LABORATORY of the department of Civil Engineering, Delft University of Technology, Delft, The Netherlands
and
INSTITUTE TNO for Building Materials and Building Structures, Rijswijk (ZH), The Netherlands.
HERON contains contributions based mainly on research work performed in these laboratories on strength of materials, structures and materials science.

Secretary:
G. J. van Alphen
Stevinweg 1
P.O. Box 5048
2600 GA Delft, The Netherlands
Tel. 0031-15-785919
Telex 38070 BITHD

HERON vol. 29 1984 no. 3

Contents

NON-ASSOCIATED PLASTICITY FOR SOILS, CONCRETE AND ROCK

P. A. Vermeer
Department of Civil Engineering, Geotechnical Laboratory
Delft University of Technology

R. de Borst
Software Engineering Department/Section DIANA
Institute TNO for Building Materials and Building Structures

NON-ASSOCIATED PLASTICITY FOR SOILS, CONCRETE AND ROCK

Summary

With reference to practical engineering problems it is shown that considerable differences may be encountered between the results from associated and those from non-associated plasticity theories. Next, the need for a non-associated plasticity theory is demonstrated by considering test results for sand, concrete and rock. Elementary material parameters are discussed such as Young's modulus and Poisson's ratio for the description of the elastic properties; and a cohesion and a friction angle for the determination of the strength. The salient difference from associated plasticity theory concerns the introduction of a dilatancy angle which controls the inelastic (plastic) volume changes. This dilatancy angle is not only a suitable parameter for the description of soils, but also appears to be useful for concrete and rock.

Basically, the paper consists of three parts as we consider three types of models of increasing complexity. The first model is a perfectly-plastic model, which employs the five aforementioned parameters. It is based on test data rather than on Drucker's hypothesis of material stability. The consequences thereof are examined. The second model is a straightforward extension of the first model by augmenting it with friction hardening and cohesion softening. This novel idea is introduced to account for the degradation of the cohesion of cemented granular materials with increasing inelastic deformation. The model is employed in an analysis which shows that plastic deformations tend to localize in thin shear bands, which may occur even before peak strength is reached. Finally, a review is given of concepts for modelling hysteresis and strain accumulation in cyclic loading. The concept of a bounding surface in addition to a yield surface is discussed and is adapted for use in a sophisticated model for loose and cemented granular materials under cyclic loading.

Non-associated plasticity for soils, concrete and rock

1 Introduction

The theory of plasticity is now well established for metals. The hypotheses which are assumed in metal plasticity are simple and supported by a large amount of experimental evidence. Further, these hypotheses provide a firm basis for an elegant mathematical theory in which a number of powerful theorems are incorporated. Here, one may think of the uniqueness theorems and the upper and lower bound theorems for the limit load in quasi-static loading (Koiter, 1960). This theory will here be referred to as the theory of associated plasticity.

Unfortunately, the fundamental hypothesis which forms the basis of associated plasticity and consequently also of the successful application of plasticity theory in the design of steel structures, does not hold for other civil-engineering materials like soils and concrete. For these materials, experiments have disproved the hypothesis of normality (postulate of material stability) as formulated by Drucker (1952, 1964). An implication thereof is that design methods for soil and concrete structures, such as slip circle methods for slopes and yield line analysis for concrete slabs, cannot rigorously be characterized as upper bound approaches. A more severe consequence is that the suitability of some constitutive models for use in finite element computations becomes questionable. Indeed, some such laws employ associated plasticity. Examples thereof are the Drucker-Prager model (1952) and the DiMaggio-Sandler model (1971). Both models are treated in the recent book by Chen (1982) on concrete plasticity. We will show that such models are not generally useful by considering results for several practical problems.

The shortcomings of associated plasticity were first recognized for soils and later also for rock and concrete. The literature thereof is dispersed over journals and congress proceedings. Yet, in recent text books it has received little attention; outstanding exceptions are the books by Salençon (1977) and Smith (1982). Many engineers and scientists have had little exposure to the theory of non-associated plasticity; others are familiar with fragments of the theory. It is for this reason that this paper not only presents novel extensions but also well-established concepts.

The paper starts with a brief explanation of the phenomenon of shear dilatancy in loose granular material (sand) or in a cemented granular material (concrete, rock). Next it is shown that a plastically volume-preserving material gives a different response upon loading than a material which exhibits plastic dilation. Differences are found both with regard to the load-deformation curve and with regard to the limit load. The fact that even limit loads may depend on the dilatancy characteristics of the granular material is known, but has as yet hardly been demonstrated by examples. Davis (1968) presented an example of compression between rough platens, and this example was also used by Zienkiewicz et al. (1975). New examples are given here. In the next

chapter typical data as obtained in triaxial tests on sand, concrete and rock are considered. It is shown that associated plasticity cannot describe such test result satisfactorily. The novel element in this chapter is the evaluation of the so-called dilatancy angle from test data.

Chapter 4 contains well-established concepts. The elastic-perfectly plastic model described here is the basis of the more sophisticated models considered in the later chapters. It is also a useful model for solving practical problems. Indeed, we have put the model into practice in many finite element calculations. In some of such problems, we encountered some unexpected effects which appeared to be consequences of non-associated plasticity. These consequences are reviewed and discussed in Chapter 5.

Chapter 6 discusses the mechanism of hardening for frictional materials, and develops some thoughts on hardening models. For concrete and rock, which possess both cohesion and internal friction, the situation is more complicated than for sand, as the hardening can in principle be applied to the cohesion as well as to the mobilised friction angle. Considering triaxial test data, we argue that friction hardening generally gives a better description of the test results than cohesion hardening, which is commonly applied to describe the hardening behaviour of metals. A particular idea, namely in which friction hardening is combined with softening on the cohesion is elaborated in the next chapter. This idea seems promising, as it is shown by a simple example that the increased ductility at higher stress levels can be accommodated very well within such an approach.

Non-associated plasticity models may give rise to non-unique limit loads and may involve unstable structural behaviour, as is shown in Chapter 5 for the perfectly-plastic model. Non-uniqueness and unstable behaviour may also be encountered for a hardening model. This will be illustrated in Chapter 8, where we will present a shear-band analysis. It is shown that non-unique solutions (bifurcations) are possible prior to peak strength. Again the theoretical analysis is accompanied by some results from numerical calculations.

The last chapter presents a general overview of plasticity models which aim at describing the stress-strain behaviour of loose granular or cemented granular materials under cyclic loading. It is argued that there exists little consensus as to which direction should be pursued, but some ideas which seem most promising are discussed in somewhat greater detail. By means of an example it is shown that such ideas may result in models which can reasonably describe the behaviour of granular materials subjected to cyclic loading.

2 The significance of dilatancy

Shear dilatancy (or dilatancy for short) of a granular material was first discussed by Reynolds (1885). Dilatancy may be described as the change in volume that is associated with shear distortion of an element in the material. Here, an element is assumed to be macroscopic and large enough to contain many particles as micro-elements. Consider for instance a pack of incompressible spheres arranged in a state of packing as dense

as possible. If any shear distortion is applied, the relative positions of the spheres must change, and the total volume of the pack must increase. Similarly, if the pack has originally been set up in a very loose state of packing, a shear distortion will cause a reduction of the volume of the pack. These volume changes are called dilatancy. It is observed in all granular materials, including cemented materials like concrete and rock.

A suitable parameter for characterizing a dilatant material is the dilatancy angle ψ. This angle was introduced by Bent Hansen (1958) and represents the ratio of plastic volume change over plastic shear strain. Strictly speaking, this definition is only exact in the case of simple shear as will be shown in Section 4.3. When testing a particular material, the dilatancy angle is found to be constant near and at peak strength. For soils the dilatancy angle is known to be significantly smaller than the friction angle. For concrete and rock the situation is very similar, as we will show in this paper.

In order to assess the importance of the dilatancy angle, some problems of practical interest will now be treated. The first problem concerns a rigid circular plate which is pushed into a granular material (insert in Fig. 2.2). A second problem concerns the penetration of a circular cone in a sand bed as illustrated in the insert of Fig. 2.3. For simplicity, the granular material is idealized by assuming a bilinear stress-strain curve as plotted in Fig. 2.1. This constitutive model involves five material parameters, namely Young's modulus E, Poisson's ratio ν, a cohesion c, an angle of internal friction ϕ, and the abovementioned angle of dilatancy ψ. The mathematical details of this model will be given in Chapter 4.

The loading of a circular foundation plate is a classical problem in soil mechanics. We performed a finite element analysis for the purpose of examining the influence of the dilatancy angle ψ. The plate is taken to be perfectly smooth and the granular material is initially stress free. The weight of this material is neglected. This problem was analysed for two different dilatancy angles, one giving no dilatancy at all (that means a plastically volume preserving model), the other giving an extremely high degree of dilatancy.

Obviously, the initial slopes of the load-displacement curves must coincide as the material behaves in an entirely elastic manner at the onset of loading. Because of stress concentrations, plastic zones will develop near the edge of the plate under continued

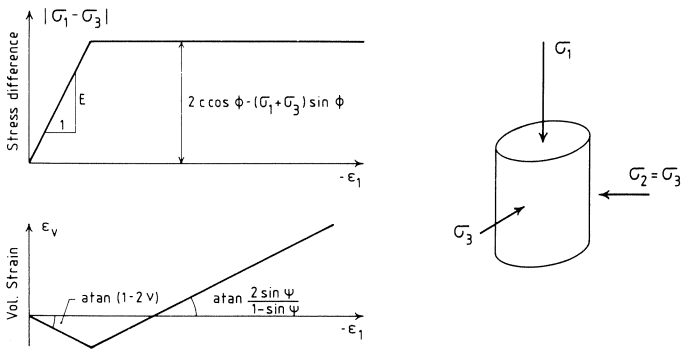

Fig. 2.1 Bilinear idealisation of triaxial test results.

loading. As will be explained in greater detail in subsequent chapters, the behaviour and the spread of the plastic zones will be influenced by dilatancy. Indeed, it can be observed from Fig. 2.2, that the load-displacement curves deviate more and more as the load increases. The response of the strongly dilatant is simply much stiffer than the response of the non-dilatant (plastically volume preserving) material. At some load level the plastic zones will have spread underneath the plate and failure will occur. Despite the differences in load-deformation behaviour, it appears that both curves yield the same failure load as indicated by the dashed line in Fig. 2.2. The computed limit load may safely be relied upon as it closely agrees with a rigid-plastic, semi-analytical solution by Cox et al. (1961). Cox solved the problem for the (strongly) dilatant material and obtained $p = 20.1c$, in which p is the average plate pressure at failure, and c is the cohesion of the material. In contrast with Cox's solution, the finite element calculation not only gives the limit load, but yields the entire load-displacement curve.

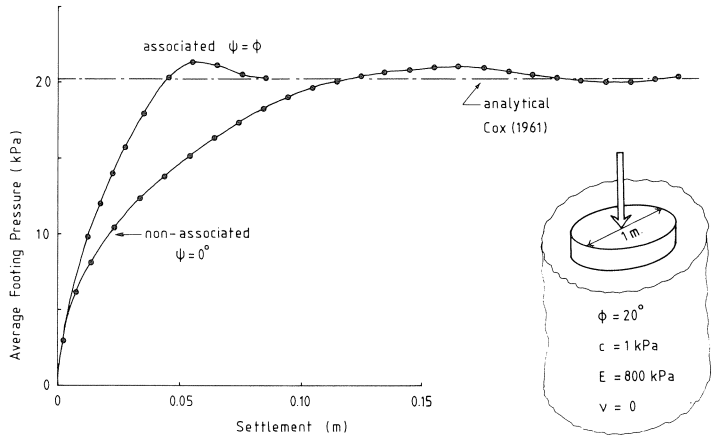

Fig. 2.2 Finite element results for plate indentation; the limit load does not depend on the dilatancy angle ψ.

The above plate loading problem is somewhat artificial as the plate was considered to be perfectly smooth. In such a situation the material can displace freely along the bottom of the plate. As a consequence, the material underneath the plate is more or less free to move towards the edge, giving an upheave of the adjacent surface. In the beginning of this section, dilatancy was defined as the change in volume associated with a shear distortion. Clearly for a given shear distortion, a material having more dilatancy will show a greater volume increase than a material showing less dilatancy. So we will generally observe that a material with a greater dilatancy angle will show a greater volume increase than a material with a small dilatancy angle. If, as in the present example, the material is free to flow away to a nearby free surface, we will only observe a somewhat stiffer behaviour for the more dilatant material, but no or virtually no effects upon the limit load. However, the situation is different when the material cannot easily be conveyed to a nearby boundary. Here, we may envisage situations such as deeply embedded anchors in soil or ribbed steel bars in massive concrete structures. When

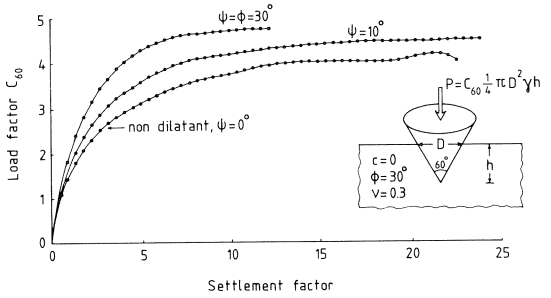

Fig. 2.3 Finite element results for cone indentation; the limit load depends on the dilatancy angle ψ.

such an anchor or metal bar is pulled out of the granular material, the limit load will certainly be influenced by the intensity of the dilatancy. For such so-called kinematically constrained problems a more dilatant material will involve a higher failure load. This phenomenon will be explained more fully in Chapter 4.

An example involving a kinematically (slightly) more constrained configuration is given in Fig. 2.3. It concerns a circular cone which is pushed into a sand bed. Several such computations were performed by Zaadnoordijk (1983). Similarly to the plate problem, the response of the material is stiffer as the dilatancy angle increase. Now the load-carrying capacity also increases. In structural mechanics kinematically constrained situations are less common than in soil mechanics. For concrete beams and slabs the dilatancy is so easily conveyed to the nearby boundaries that the dilatancy angle does not influence the failure loads. For such one- and two-dimensional structures a limit analysis can be performed on the basis of strength parameters alone, and the results of such analyses can still be used with confidence in most cases, despite the fact that upper and lower bound theorems (see Koiter, 1960) are strictly speaking no longer valid. For truly three-dimensional structures however, we may again expect that the dilatancy angle affects the load-carrying capacity. This is exemplified by the dome structure of Fig. 2.4, which was analysed using the DIANA computer program. The other sample problems were solved using the PLAXIS finite element program (De Borst and Vermeer, 1984).

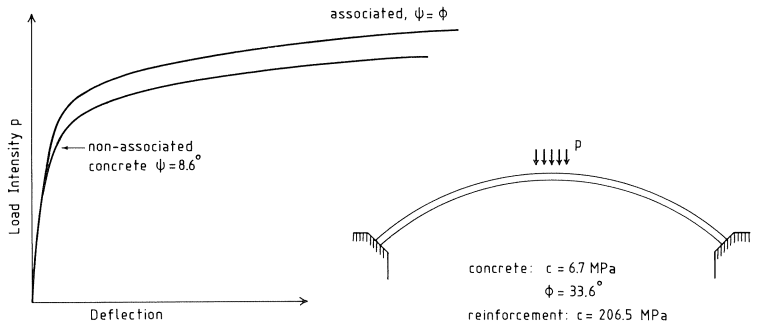

Fig. 2.4 Finite element results for a dome structure; associated plasticity underestimates the deflection.

3 Triaxial compression tests and elementary parameters

Uniaxial compression tests are probably the most widely used tests for concrete. A simple extension of this type of test is the triaxial compression test, which has found widespread application for soil testing. Ideally, a triaxial test should permit independent control of all three principal stresses (Fig. 3.1a), so that general states of stress can be examined. Such tests, however, require rather sophisticated apparatus, which precludes the use thereof for other than research purposes. Therefore, cylindrical specimens are tested in the usual triaxial apparatus. These specimens are sealed in a rubber watertight membrane and are enclosed in a cell in which the specimens can be subjected to a fluid pressure. Next, the axial stress is increased, so that it becomes the major compressive stress. The other stresses remain equal to the cell pressure. Thus, a uniaxial test can be conceived as a triaxial test without cell pressure.

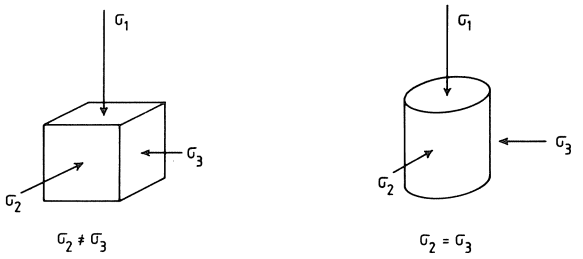

Fig. 3.1 Cuboidal specimen for true triaxial and cylindrical specimen for common triaxial apparatus.

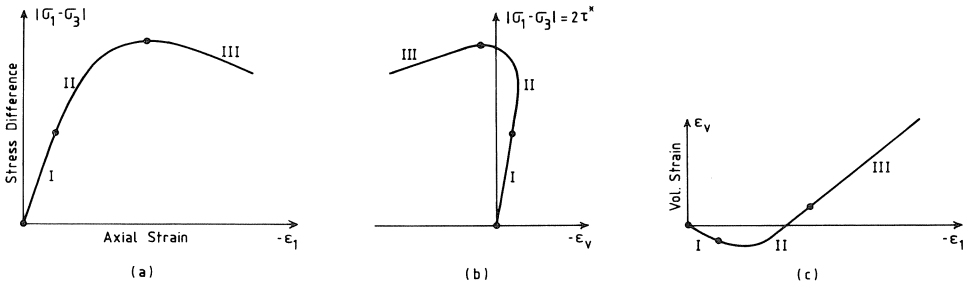

Fig. 3.2 Typical triaxial test results for a loose or a cemented granular material.

Under compressive stress the test results for soils, rock and concrete are essentially similar. A stress-strain curve typical of the behaviour in a standard triaxial test is shown in Fig. 3.2a. The curve consists of three parts. Section I is nearly linear, section II is of a monotonically decreasing slope and the post-peak region III is characterized by a negative slope of the curve. In terms of plasticity theory we speak of elastic behaviour, hardening behaviour, and softening behaviour respectively. For cracked rock the stress-strain curve may initially be concave due to the closing of micro-cracks in the beginning of loading (see Fig. 3.3).

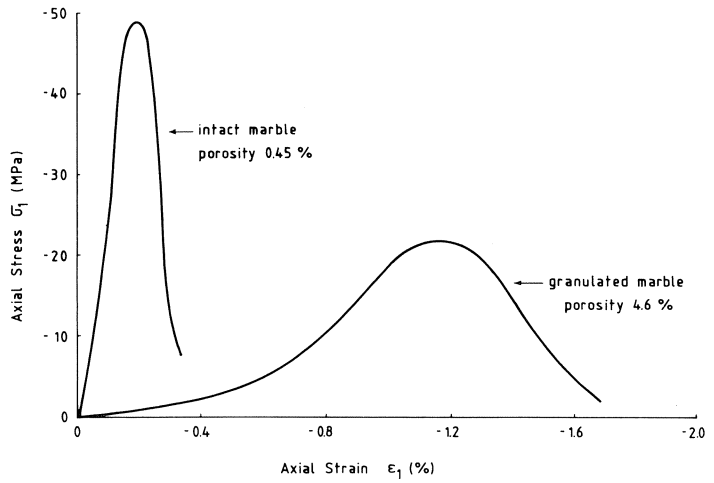

Fig. 3.3 Uniaxial compression test results for rock after Michelis (1981).

In the following we will discuss the stress-strain curve in greater detail. The novel element in our treatment is the introduction of an equation for the evaluation of the dilatancy angle ψ from triaxial test data. Using this equation we will show that we need non-associated plasticity theory. At present there is much debate on the need of non-associated models for concrete. Chen (1982) argues that there is very little experimental evidence to decide in favour of either associated or non-associated plasticity. By an evaluation of existing test data, we will show the need for non-associated plasticity.

3.1 *The elastic region*

At the onset of loading, the behaviour of a specimen may be approximated as elastic, as all deformations are recovered upon unloading. Here, a loading-unloading cycle produces so little hysteresis that energy dissipative processes are negligible. Hence there is little or no microcracking in a concrete specimen and hardly any particle rearrangement in a soil specimen. Consequently, Hooke's law may be applied. If we assume isotropy, two constants then suffice for the description of the material behaviour, namely Young's modulus E and Poisson's ratio ν.

For concrete, the values for Young's modulus are in the range between 20 and 40 GPa, which is about a thousand times larger than the values which are common for sand. Young's modulus of rock may either approach the typical values for sand or exceed values for concrete, depending on the porosity of the material. Better agreement exists for Poisson's ratio. For concrete, most reported values are in the range 0.15 to 0.2. For soils, they are in the somewhat wider range of $0.0 < \nu < 0.3$. Poisson's ratio can only be determined if both the axial strain and the lateral strain are measured. In soil testing, the lateral strain is seldom measured directly. The volumetric strain is measured instead.

3.2 *The hardening regime*

The initiation of the hardening behaviour is gradual and not clearly defined. In this stage of the test the deformation becomes more and more inelastic due to micro-cracking in concrete and rock and due to particle sliding in soil specimen. Here, the use of non-linear elasticity would lead to an inconsistent and inaccurate description, as such theories predict continuing contraction of the specimen under continued loading in compression. Such a prediction is disproved by experimental evidence (see Fig. 3.2b), which shows a dilatant volume increase at subsequent loading. This phenomenon is caused by frictional sliding, either along particles or along micro-cracks (see Fig. 3.4).

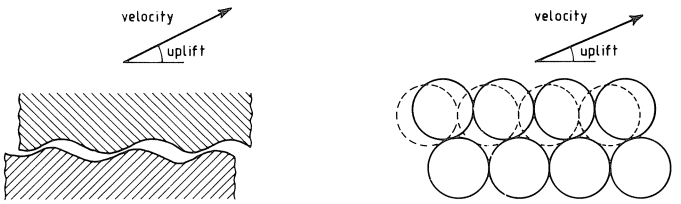

Fig. 3.4 Sliding at microcracks and sliding between groups of particles; both cases give dilation.

Figs. 3.6 and 3.7 show that such a dilatant volume increase is characteristic not only of sandy soils, but also of concrete and rocks. Anticipating a more rigorous discussion on dilatancy, we will now introduce some concepts from plasticity theory which are relevant to the description of this phenomenon. To this end, it is first necessary to introduce a basic assumption from plasticity theory:

$$\dot{\boldsymbol{\varepsilon}} = \dot{\boldsymbol{\varepsilon}}^{e} + \dot{\boldsymbol{\varepsilon}}^{p} \tag{3.1}$$

This equation states that the total strain rate is the sum of an elastic and a plastic contribution. As in the sequel, the superscripts e and p denote elastic and plastic quantities respectively, while a symbol in bold type means that we are dealing with a column matrix. A dot above a symbol implies the material time derivative. For readers not familiar with plasticity theory this dot may be somewhat confusing, because in common plasticity theory time is not taken into account, but merely serves as a parameter which controls the sequence of the loading process. Consequently, viscous effects are not included in this formation, so that we are essentially dealing with an inviscid material model.

Near the end of the hardening regime the axial stress hardly increases and this means that the elastic strain rate is almost zero, so that all further strain increments are of a plastic nature. Then the fundamental observation is that there exists a linear relation between the volume change and the change of the axial strain (Fig. 3.2c); the so-called rate of dilation is found to be a constant. We formulate this observation by means of the equations:

$$\sin \psi = \frac{\dot{\varepsilon}_v^p}{-2\dot{\varepsilon}_1^p + \dot{\varepsilon}_v^p} \tag{3.2}$$

$$\dot{\varepsilon}_v = \dot{\varepsilon}_1 + \dot{\varepsilon}_2 + \dot{\varepsilon}_3 \tag{3.3}$$

where ψ is a constant, which is commonly called the dilatancy angle. In soil mechanics literature the dilatancy angle is defined for plane strain conditions, using another equation. In Section 4.4. it will be shown that the above equation holds for triaxial compression conditions as well as for plane strain conditions.

3.3 *The softening regime*

Stress-strain curves from conventional triaxial tests show peaks; these are strongly marked for dense sands and also for rocks and concrete when tested at low confining pressures, but are very smooth in the case of loose sands and also for concrete and rock when tested at high confining pressures. The marked peaks are partly caused by thin shear bands (or faults), which separate the specimen in two more or less rigid bodies. For such macroscopic non-uniform deformations the strain measurements are no longer objective. The situation is comparable to the necking of a steel bar in a tensile test, where the length of the bar influences the measured strain. Similarly, the faulting or bulging of specimens in triaxial compression tests leads to marked peaks and non-objective strain measurements. As a consequence, the final sections of the stress-strain curves in the Figs. 3.2a and 3.2b cannot be used to derive material constants. The axial strain-volumetric strain curve of Fig. 3.2c is much more useful. Indeed, the magnitude of the strain increments is incorrectly measured, but the strain rate ratio is not so strongly affected by the localization into a shear band. Hence the dilatancy angle can be measured with acceptable accuracy despite the non-uniformity of the deformation.

Apparently, common triaxial compression tests are not reliable in the softening regime due to the fact that it is virtually impossible to retain a uniformly deformed specimen in this range. For this reason, special tests with more objective strain measurements have recently been performed on a very dense sand (Hettler and Vardoulakis, 1984). The stress-strain curves resulting from these tests show a very smooth peak as shown in Fig. 3.5a. This strongly indicates that the marked peaks for dense sand which are found in common triaxial tests are indeed largely caused by shear bands and other non-uniform deformations. For concrete the situation is more complicated, since tensile-type fractures occur when the specimen is tested at low cell pressures. However, at higher cell pressures concrete and soils again show similar characteristics. An analytical examination of shear-band formation will be given in Chapter 8.

In Fig. 3.5b, an axial strain-volumetric strain curve is given for a dense sand. From this figure we obtain a slope of -0.7 for $\dot{\varepsilon}_v^p/\dot{\varepsilon}_1^p$ which may be substituted into equation (3.2) to obtain $\psi = 15°$. This value is typical of a very dense sand, whereas loose sands have dilatancy angles of just a few degrees, and normally consolidated clays show no dilatancy at all.

For concrete and rocks we observe essentially the same trend, as can be seen in Figs.

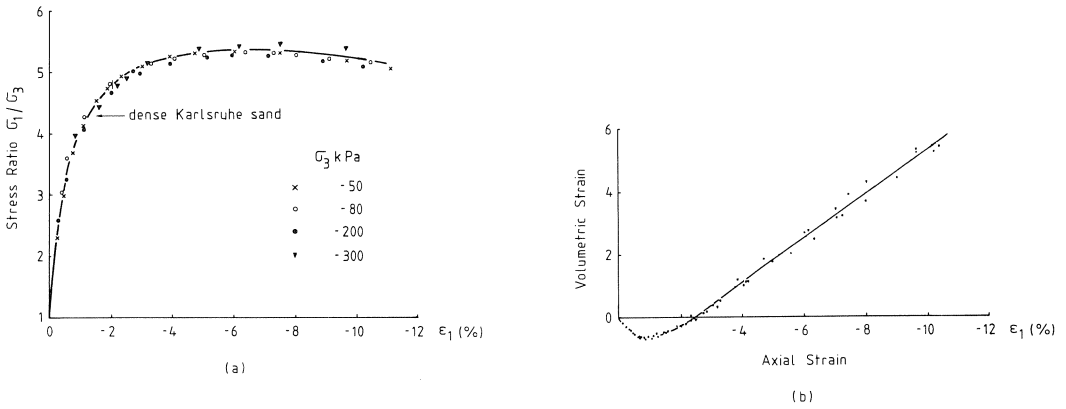

Fig. 3.5 Triaxial test results for a dense sand after Hettler and Vardoulakis (1984).

3.6 and 3.7, in which plots similar to the one in Fig. 3.5b are displayed for some rocks and concrete. Applying formula (3.2), we obtain values for the dilatancy angle ranging from 12° to 20° for the rocks. Michelis (1981) also presents data for cell pressures of about 200 MPa showing dilatancy angles of 6° to 9° at extremely large pressures. The concrete data of Fig. 3.7 can be worked out to give $\psi = 13°$. Like that of rock and soils, the dilatancy of concrete vanishes at high confining pressures. This trend is observed in data given by Traina (1983) for a low-strength concrete. Hence, it appears that all values for the dilatancy angle are approximately between 0° and 20° whether we are dealing with soils, concrete or rocks. Finally, it is remarked that a material can of course not

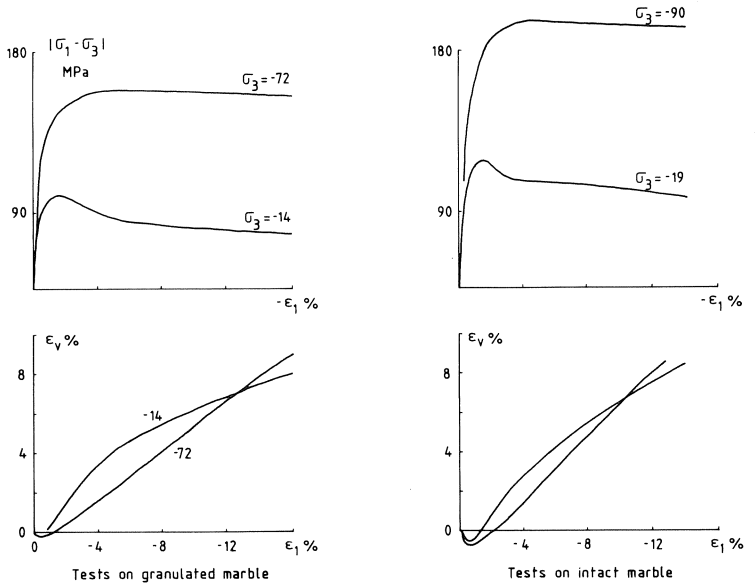

Fig. 3.6 Triaxial test results for rocks after Michelis (1981); in contrast with Fig. 3.3 there is no basic difference between intact and micro-cracked rock.

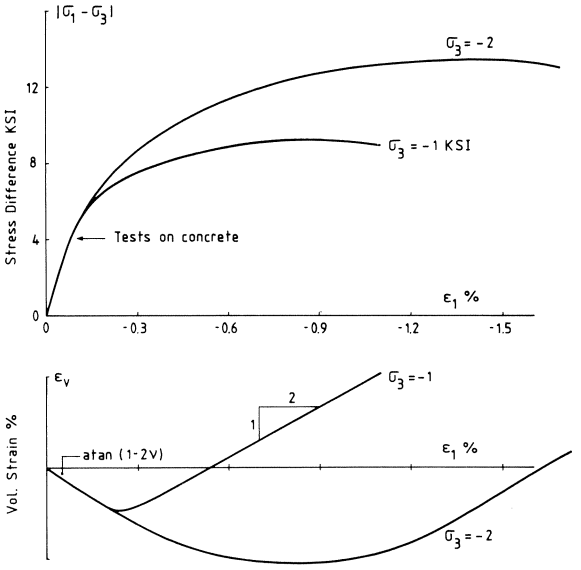

Fig. 3.7 Replot of triaxial test result for a high-strength concrete after Green and Swanson (1973).

dilate infinitely. Indeed, after intense shearing the dilatancy angle gradually vanishes and any subsequent shearing causes no more volume changes.

3.4 *Strength parameters*

Having considered deformation parameters such as E, ν and ψ, we will now consider strength parameters. From triaxial tests performed with different cell pressures it is found that the peak strength increases as a function of the cell pressure. From an engineering point of view a linear strength criterion $\sigma_1 = a + b\sigma_3$ is usually accurate enough. This criterion can be rewritten as:

$$|\sigma_1 - \sigma_3| + (\sigma_1 + \sigma_3) \sin \phi - 2c \cos \phi \leqslant 0 \tag{3.4}$$

with c the cohesion of the material and ϕ the angle of internal friction. For soils, most values for the angle of internal friction are between 15° and 45°, where values up to 30° are typical of clays and the larger values are found for sands. For concrete, most reported values are in the range of $30° < \phi < 35°$. Because of this rather narrow range the cohesion is almost entirely determined by the uniaxial compression strength

$$c = -a \frac{1 - \sin \phi}{2 \cos \phi} \approx -0.3a \tag{3.5}$$

Note that compressive stresses are treated as negative, so that the constant a in the strength criterion $\sigma_1 = a + b\sigma_3$ is negative. The data of Fig. 3.5a are well fitted by the parameters $a = 0$ and $b = 5.3$. These values may be used to calculate $c = 0$ and $\phi = 43°$, being typical of a very dense sand.

It thus appears that the friction angle is generally much greater than the dilatancy angle, whether we consider soils, concretes or rocks. This observation implies that a non-associated plasticity theory should be employed for these materials.

4 The non-hardening model

For stability analyses a non-hardening model (Fig. 2.1) leads to results that are often as good as those obtained by the use of more complicated material models. Since factors such as simplicity and computer-run time must be considered, an efficient computer program should incorporate a non-hardening model as a first option. We will therefore first elaborate a model which neglects the effect of hardening or softening of the material. In the first sections of this chapter we will confine ourselves to conditions of plane strain. In soil mechanics, plane-strain situations (dams, sheets pilings, retaining walls) are as common as plane-stress situations are in structural mechanics (beams, slabs, shells). The restriction to plane-strain conditions is not essential, as it will be shown in Section 4.4 that the model can easily be extended to general three-dimensional stress states.

This chapter is of a somewhat elementary nature. It is included for readers who are not very familiar with non-associated plasticity theory.

4.1 *General equations for plane strain conditions*

The definition of plane deformations is given by the following equation for the matrix of strain components

$$\begin{bmatrix} \varepsilon_{xx} & \frac{1}{2}\gamma_{xy} & \frac{1}{2}\gamma_{xz} \\ \frac{1}{2}\gamma_{yx} & \varepsilon_{yy} & \frac{1}{2}\gamma_{yz} \\ \frac{1}{2}\gamma_{zx} & \frac{1}{2}\gamma_{zy} & \varepsilon_{zz} \end{bmatrix} = \begin{bmatrix} \varepsilon_{xx} & \frac{1}{2}\gamma_{xy} & 0 \\ \frac{1}{2}\gamma_{yx} & \varepsilon_{yy} & 0 \\ 0 & 0 & 0 \end{bmatrix} \tag{4.1}$$

These strain components refer to a rectangular Cartesian coordinate system x,y,z. For such two-dimensional states of strain it is useful to introduce the computer oriented notation

$$\begin{aligned} \boldsymbol{\varepsilon} &= (\varepsilon_{xx} \quad \varepsilon_{yy} \quad \gamma_{xy} \quad \varepsilon_{zz})^T \\ \boldsymbol{\sigma} &= (\sigma_{xx} \quad \sigma_{yy} \quad \sigma_{xy} \quad \sigma_{zz})^T \end{aligned} \tag{4.2}$$

where the superscript T denotes a transpose. The general rule of plasticity is that the strain rate $\dot{\boldsymbol{\varepsilon}}$ is resolved into an elastic contribution $\dot{\boldsymbol{\varepsilon}}^e$ and a plastic contribution $\dot{\boldsymbol{\varepsilon}}^p$ (see equation (3.1)). Hooke's law is used for the elastic strain rate, giving

$$\begin{bmatrix} \dot{\sigma}_{xx} \\ \dot{\sigma}_{yy} \\ \dot{\sigma}_{xy} \\ \dot{\sigma}_{zz} \end{bmatrix} = \frac{E}{(1-2\nu)(1+\nu)} \begin{bmatrix} 1-\nu & \nu & 0 & \nu \\ \nu & 1-\nu & 0 & \nu \\ 0 & 0 & \frac{1}{2}-\nu & 0 \\ \nu & \nu & 0 & 1-\nu \end{bmatrix} \begin{bmatrix} \dot{\varepsilon}^e_{xx} \\ \dot{\varepsilon}^e_{yy} \\ \dot{\gamma}^e_{xy} \\ \dot{\varepsilon}^e_{zz} \end{bmatrix} \tag{4.3}$$

or in abbreviated symbolic notation

$$\dot{\boldsymbol{\sigma}} = \mathbf{D}\dot{\boldsymbol{\varepsilon}}^{e} \tag{4.4}$$

Using equation (3.1) we obtain:

$$\dot{\boldsymbol{\sigma}} = \mathbf{D}(\dot{\boldsymbol{\varepsilon}} - \dot{\boldsymbol{\varepsilon}}^{p}) \tag{4.5}$$

Obviously, this equation is incomplete as it has to be complemented by an expression for the plastic strain rate. This matter will be discussed in the next sections.

4.2 *The yield function f*

We will consider a macroscopically homogeneous element of granular material. The element is in static equilibrium and uniformly stressed as is shown in Fig. 4.1a. The shear component and the normal component of the traction on an arbitrary surface element are denoted as τ_n and σ_n respectively. The Mohr-Coulomb strength criterion postulates, in analogy with the law of dry friction between two sliding surfaces,

$$|\tau_n| \leqslant c - \sigma_n \tan \phi \tag{4.6}$$

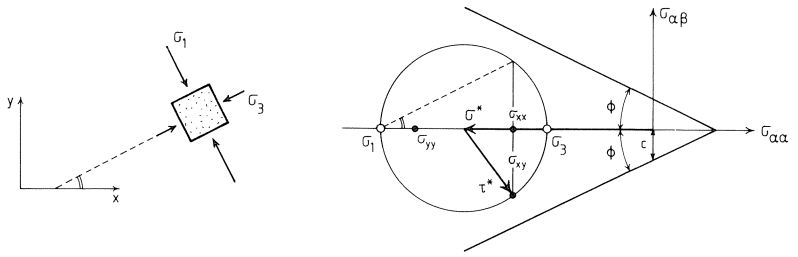

Fig. 4.1 Coordinate system and stress circle for a material element in plane state of strain.

for any particular surface element. Tensile stress components are treated as positive, as is usual in continuum mechanics. The Mohr-Coulomb criterion can also be formulated in terms of stress tensor components. Here one should realize that the criterion simply means that all possible stress circles are bounded by the cone-type envelope in Fig. 4.1b. This can be expressed by the equivalent criterion

$$\tau^* - \sigma^* \sin \phi - c \cos \phi \leqslant 0 \tag{4.7}$$

where σ^* is the centre of the stress circle,

$$\sigma^* = -\tfrac{1}{2}(\sigma_{xx} + \sigma_{yy}) \tag{4.8}$$

and τ^* is the radius of the stress circle,

$$\tau^* = \sqrt{\tfrac{1}{4}(\sigma_{xx} - \sigma_{yy})^2 + \sigma_{xy}^2} \tag{4.9}$$

Note that τ^* is half the difference between σ_1 and σ_3, so that the equations (3.4) and (4.7) are identical. For $\phi = 0°$ the Coulomb criterion reduces to the well-known Tresca criterion for metals. Tresca proposed his criterion in 1864, and his ideas were probably influenced by the earlier work of Coulomb.

In plasticity literature a so-called yield function (often denoted by the symbol f) is commonly employed to distinguish plastic from elastic states. If we define for the Mohr-Coulomb criterion:

$$f = \tau^* - \sigma^* \sin \phi - c \cos \phi \tag{4.10}$$

we see that equation (4.7) can be abbreviated as:

$$f \leqslant 0 \tag{4.11}$$

The function f is negative as long as the stress circle makes no contact with the Coulomb envelope, while it vanishes when they touch. The material cannot sustain a stress circle that intersects the envelope (this would imply $f > 0$). Hence, a material element is said to be in an elastic state if $f < 0$, and in a plastic state when $f = 0$. Obviously, an element may pass from an elastic state to a plastic state and vice versa. For plastic yielding, the element needs to be in a plastic state ($f = 0$), and to remain in a plastic state ($\dot{f} = 0$); otherwise the plastic strain rate vanishes. Hence

$$\dot{\boldsymbol{\varepsilon}}^{\mathrm{p}} = 0 \quad \text{for} \quad f < 0 \quad \text{or} \quad (\dot{f} < 0 \quad \text{and} \quad f = 0) \tag{4.12}$$

otherwise there is yielding. Thus, the first condition refers to an element in an elastic state, while the second condition refers to an element which passes from a plastic state to an elastic state (unloading).

4.3 *Flow rule and plastic potential*

In contrast with elasticity theory, where a one-to-one correspondence exists between the total stresses and the total (elastic) strains, such a unique relation does not exist between the plastic strains and the stresses. Instead, the plastic strain rates are assumed to be derived from a scalar function g of the stresses as follows:

$$\dot{\boldsymbol{\varepsilon}}^{\mathrm{p}} = \lambda \frac{\partial g}{\partial \boldsymbol{\sigma}} \tag{4.13}$$

Here, λ is a non-negative multiplier if plastic loading occurs ($f = 0$ and $\dot{f} = 0$), whereas it vanishes under condition (4.12). It is emphasized that the multiplier λ has no physical meaning at all. It can for instance not be identified with a viscosity. How this multiplier is computed will be considered in Section 4.5.

The function g is called the plastic potential function. For planar deformations of granular material, whether cemented or not, a suitable definition for g is (Radenkovic, 1961):

$$g = \tau^* - \sigma^* \sin \psi + \text{constant} \tag{4.14}$$

where ψ is the dilatancy angle as discussed in the preceding chapters. This particular plastic potential closely resembles the (Mohr-Coulomb) yield function f, the only difference being that the angle of internal friction ϕ in f is replaced by the dilatancy angle ψ. Differentiating g with respect to the stresses, we obtain the flow rule

$$\begin{bmatrix} \dot{\varepsilon}^p_{xx} \\ \dot{\varepsilon}^p_{yy} \\ \dot{\gamma}^p_{xy} \\ \dot{\varepsilon}^p_{zz} \end{bmatrix} = \lambda \begin{bmatrix} \partial g/\partial \sigma_{xx} \\ \partial g/\partial \sigma_{yy} \\ \partial g/\partial \sigma_{xy} \\ \partial g/\partial \sigma_{zz} \end{bmatrix} = \lambda \begin{bmatrix} (\sigma_{xx} - \sigma_{yy})/2\tau^* + \sin\psi \\ -(\sigma_{xx} - \sigma_{yy})/2\tau^* + \sin\psi \\ 2\sigma_{xy}/\tau^* \\ 0 \end{bmatrix} \tag{4.15}$$

In actual computations we thus need the flow rule rather than the plastic potential function g itself.

In order to understand this flow rule, it is helpful to consider the equation

$$\sin\psi = \dot{\varepsilon}^p_v/\dot{\gamma}^p \tag{4.16}$$

which follows from the flow rule using

$$\begin{aligned} \dot{\varepsilon}^p_v &= \dot{\varepsilon}^p_{xx} + \dot{\varepsilon}^p_{yy} + \dot{\varepsilon}^p_{zz} = \dot{\varepsilon}^p_{xx} + \dot{\varepsilon}^p_{yy} \\ \dot{\gamma}^p &= \sqrt{(\dot{\varepsilon}^p_{xx} - \dot{\varepsilon}^p_{yy})^2 + (\dot{\gamma}^p_{xy})^2} \end{aligned} \tag{4.17}$$

The definition of $\dot{\gamma}^p$ compares with definition (4.9) of the shear stress and $\dot{\gamma}^p$ is referred to as the rate of plastic distortion. The above equations give the meaning of the dilatancy angle. This angle sets the ratio of two plastic strain rates, namely the rate of plastic volumetric strain and the rate of plastic distortion. This definition is in agreement with definition (3.2), as we can also write:

$$\dot{\gamma}^p = |\dot{\varepsilon}^p_3 - \dot{\varepsilon}^p_1|$$

Using the additional equation $\dot{\varepsilon}^p_2 = 0$, we can derive equation (3.2) from equation (4.16).

The physical meaning of ψ can be even better understood by considering a shear box test as indicated in Fig. 4.2. The material at the interface between the two halves of the box forms a thin rupture zone. For most of this shear zone there will be no parallel strain, that is

$$\dot{\varepsilon}_{xx} = \dot{\varepsilon}^e_{xx} + \dot{\varepsilon}^p_{xx} = 0$$

In the beginning of the shear-box test the parallel stress σ_{xx} may change to cause some

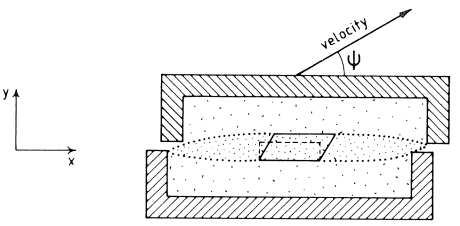

Fig. 4.2 The model predicts an uplift angle ψ for shear bands.

elastic strains, but finally σ_{xx} will be constant so that both the elastic contribution and the plastic contribution vanish:

$$\dot{\varepsilon}^{p}_{xx} = 0 \qquad \dot{\varepsilon}^{p}_{yy}/\dot{\gamma}^{p}_{xy} = \tan \psi$$

The latter equation is obtained by substituting the former in the equations (4.16) and (4.17). Let $\dot{v}$ be the vertical velocity and $\dot{u}$ the horizontal velocity of a material point in a rupture zone. We then find

$$\dot{v}/\dot{u} = \tan \psi$$

Thus, ψ is the uplift angle in a shear band.

4.4 *Extension to three-dimensional stress states*

In the foregoing, the discussion concentrated on planar deformations. Especially for the Mohr-Coulomb failure criterion, extension to three-dimensional stress states is straightforward, although particular difficulties may occur at some points of the yield surface. For this purpose, we first rewrite the yield function in terms of principal stresses. Noting that we have for the major (σ_1) and minor (σ_3) principal stress respectively

$$\sigma_1 = -(\sigma^* + \tau^*) \qquad \sigma_3 = -(\sigma^* - \tau^*)$$

we can replace equation (4.7) by the equivalent formulation

$$f = \tfrac{1}{2}(\sigma_3 - \sigma_1) + \tfrac{1}{2}(\sigma_3 + \sigma_1) \sin \phi - c \cos \phi \tag{4.18}$$

Again, yielding now occurs if $f = 0$ and $\dot{f} = 0$.

The yield condition $f = 0$ describes an angular yield surface in the principal stress space as shown in Fig. 4.3. Many researchers have performed true-triaxial tests for the purpose of establishing the yield surface empirically. Unfortunately, the various test

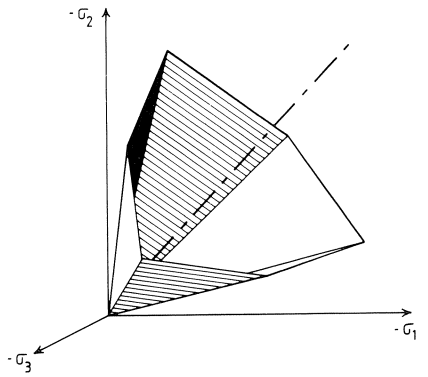

Fig. 4.3 Mohr-Coulomb yield surface in principal stress space.

results give somewhat different surfaces. It thus seems that the test results are influenced by the type of triaxial apparatus. Some devices have stiff platens on all six sides of the specimen, other have flexible fluid bags on the sides or a combination of both. We consider those types of apparatus which have the same conditions on all sides of the specimen to be most reliable. Test results for sand which were obtained by such an apparatus, have amongst others been published by Goldscheider (1984). They are represented by the dots in Fig. 4.4.a. The experimental results hardly deviate from the Coulomb surface. Experiments on concrete (see for instance Gerstle et al., 1978) show the same trend, although more curvature is found (Newman, 1979). For most engineering purposes, however, the observed deviations from the Coulomb surface are not large enough to introduce another, more complicated surface. Note that Figs. 4.3 and 4.4 are such that σ_2 is not necessarily the intermediate principal stress.

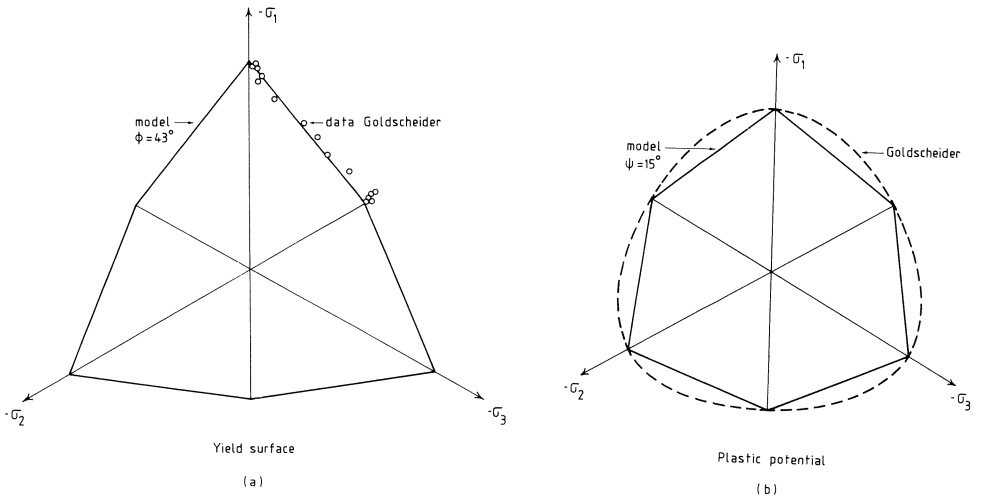

Fig. 4.4 Model versus true-triaxial test data for a dense sand.

It is seen from equation (4.18) that the intermediate principal stress (σ_2) does not influence the conditions for yielding. This property is a notable characteristic of the Mohr-Coulomb failure criterion. Moreover, the flow rule for the Mohr-Coulomb (and also for the derived Tresca) criterion predicts that there is no plastic straining in the direction of the intermediate principal stress. This can be deduced by writing the plastic potential (4.14) in terms of principal stresses also. Similarly to equation (4.18), we obtain:

$$g = \tfrac{1}{2}(\sigma_3 - \sigma_1) + \tfrac{1}{2}(\sigma_3 + \sigma_1) \sin \psi + \text{constant} \tag{4.19}$$

Differentiating this with respect to the principal stresses, we obtain for the principal plastic strain rates

$$\begin{bmatrix} \dot{\varepsilon}_1^p \\ \dot{\varepsilon}_2^p \\ \dot{\varepsilon}_3^p \end{bmatrix} = \lambda \begin{bmatrix} -\frac{1}{2}(1-\sin\psi) \\ 0 \\ \frac{1}{2}(1+\sin\psi) \end{bmatrix} \tag{4.20}$$

which proves the assertion.

The observation that the intermediate principle stress does not influence the Mohr-Coulomb yield criterion makes a generalization to three-dimensional stress states fairly straightforward. For the three-dimensional situation, the stress vector has the components

$$\mathfrak{\sigma} = (\sigma_{xx} \quad \sigma_{yy} \quad \sigma_{zz} \quad \sigma_{xy} \quad \sigma_{yz} \quad \sigma_{zx})^T \tag{4.21}$$

Similarly, the strain vector has the components:

$$\mathfrak{\varepsilon} = (\varepsilon_{xx} \quad \varepsilon_{yy} \quad \varepsilon_{zz} \quad \gamma_{xy} \quad \gamma_{yz} \quad \gamma_{zx})^T \tag{4.22}$$

In a similar way, the elasticity matrix D can be adjusted to form a $6 * 6$ matrix instead of a $4 * 4$ matrix. For any given stress state $\mathfrak{\sigma}$, we can compute the principal stresses σ_1, σ_2, σ_3, and arrange them such that

$$\sigma_1 \leqslant \sigma_2 \leqslant \sigma_3$$

Next, we can use σ_1 and σ_3 and substitute them into the yield condition (4.18) in order to check whether plasticity occurs. If this happens to be the case, equation (4.20) can be used to compute the principal plastic strain rates.

In reality, we are not so much interested in the principal plastic strain rates, but merely in the ordinary plastic strain rates, as we wish to keep track of the direction in which plastic straining occurs in the Cartesian x, y, z-space. To this end, we express the quantities σ^* and τ^* in the stress invariants p, J_2 and θ;

$$\sigma^* = \sqrt{J_2}\cos\theta - p$$

$$\tau^* = \sqrt{\tfrac{1}{3}J_2}\sin\theta$$

where the invariants, p, J_2 and θ are defined as:

$$p = \tfrac{1}{3}(\sigma_1 + \sigma_2 + \sigma_3)$$

$$J_2 = \tfrac{1}{6}[(\sigma_1 - \sigma_2)^2 + (\sigma_2 - \sigma_3)^2 + (\sigma_3 - \sigma_1)^2]$$

$$\sin 3\theta = -\frac{\sqrt{3}}{2}\frac{(\sigma_1 - p)(\sigma_2 - p)(\sigma_3 - p)}{J_2\sqrt{J_2}}$$

Using these expressions for σ^* and τ^*, the plastic potential now becomes:

$$g = \sqrt{J_2}\cos\theta - [\sqrt{\tfrac{1}{3}J_2}\sin\theta - p]\sin\psi + \text{constant} \tag{4.23}$$

from which the plastic strain rates can be derived by differentiation. Goldscheider (1984) measured the direction of the plastic strain increment slightly prior to peak strength. Using this data, we derived the dashed plastic potential curve in Fig. 4.4b. It is fairly well fitted by the angular curve for g which is defined by equation (4.23).

A complication arises if two of the principal stresses are equal (either σ_1 and σ_2 or σ_2 and σ_3). Suppose that we have $\sigma_2 = \sigma_3$, which happens to be the case in common triaxial tests. Then we have two yield conditions which vanish:

$$f_1 = \tfrac{1}{2}(\sigma_3 - \sigma_1) + \tfrac{1}{2}(\sigma_3 + \sigma_1) \sin \phi - c \cos \phi = 0$$

$$f_2 = \tfrac{1}{2}(\sigma_2 - \sigma_1) + \tfrac{1}{2}(\sigma_2 + \sigma_1) \sin \phi - c \cos \phi = 0$$

At such a point, at which yielding occurs according to two yield conditions, the total plastic strain rate can be conceived to be the sum of the individual contributions of either of the two flow rules (Koiter, 1960). We thus have

$$\dot{\boldsymbol{\varepsilon}}^p = \lambda_1 \frac{\partial g_1}{\partial \boldsymbol{\sigma}} + \lambda_2 \frac{\partial g_2}{\partial \boldsymbol{\sigma}} \tag{4.24}$$

so that we have to determine two multipliers λ_1 and λ_2. The plastic potential functions g_1 and g_2 are defined in analogy with f_1 and f_2:

$$g_1 = \tfrac{1}{2}(\sigma_3 - \sigma_1) + \tfrac{1}{2}(\sigma_3 + \sigma_1) \sin \psi + \text{constant}$$

$$g_2 = \tfrac{1}{2}(\sigma_2 - \sigma_1) + \tfrac{1}{2}(\sigma_2 + \sigma_1) \sin \psi + \text{constant}$$

When using these functions, it follows from equation (4.24) that

$$\dot{\varepsilon}_1^p = \tfrac{1}{2}(\lambda_1 + \lambda_2)(-1 + \sin \psi) \qquad \dot{\varepsilon}_v^p = (\lambda_1 + \lambda_2) \sin \psi$$

and consequently

$$\sin \psi = \dot{\varepsilon}_v^p / (-2\dot{\varepsilon}_1^p + \dot{\varepsilon}_v^p)$$

How such corner points are to be treated in a computer program, is beyond the scope of the present paper. It is merely noted that several approaches are possible. One of the classical approaches is due to Nayak and Zienkiewicz (1972) and consists in using only one yield function in combination with a rounding off procedure for points at which two planes of the yield function meet (so-called corner points). The authors use a different procedure in which equation (4.24) is incorporated exactly. For a detailed treatment thereof, the reader is referred to De Borst (1982a, 1982b).

4.5 *The incremental stress-strain relation*

In order to express the constitutive model in a matrix equation, we substitute equation (4.13) in (4.5) to obtain:

$$\dot{\boldsymbol{\sigma}} = \mathbf{D}\dot{\boldsymbol{\varepsilon}} - \lambda \mathbf{a} \qquad \mathbf{a} = \mathbf{D} \frac{\partial g}{\partial \boldsymbol{\sigma}} \tag{4.25}$$

where we recall that λ equals zero for elastic states and for unloading. For loading ($f = 0$ and $\dot{f} = 0$) the multiplier λ can be calculated from the condition that an element remains

in a plastic state when it yields. For a non-hardening material this so-called consistency condition is written as

$$\dot{f}=\frac{\partial f}{\partial \sigma_{xx}}\dot{\sigma}_{xx}+\frac{\partial f}{\partial \sigma_{yy}}\dot{\sigma}_{yy}+\frac{\partial f}{\partial \sigma_{xy}}\dot{\sigma}_{xy}+\frac{\partial f}{\partial \sigma_{zz}}\dot{\sigma}_{zz}=0$$

or in matrix notation

$$\dot{f}=\frac{\partial f^{T}}{\partial \boldsymbol{\sigma}}\dot{\boldsymbol{\sigma}}=0 \tag{4.26}$$

The expression for λ is now obtained by substituting equation (4.25) into the consistency condition. This gives

$$\dot{f}=\mathbf{b}^{T}\dot{\boldsymbol{\sigma}}-\lambda d=0 \tag{4.27}$$

where

$$\mathbf{b}^{T}=\left(\mathbf{D}\frac{\partial f}{\partial \boldsymbol{\sigma}}\right)^{T}=\frac{\partial f^{T}}{\partial \boldsymbol{\sigma}}\mathbf{D} \tag{4.28}$$

$$d=\frac{\partial f^{T}}{\partial \boldsymbol{\sigma}}\mathbf{a} \tag{4.29}$$

These equations do not seem to be very tractable. This is not true as for the Mohr-Coulomb failure condition for instance we can easily deduce that

$$d=G\left(1+\frac{\sin\psi\sin\phi}{1-2\nu}\right)$$

where G is the elastic shear modulus. The stress-strain law is finally obtained by substituting the expression for λ in equation (4.25):

$$\dot{\boldsymbol{\sigma}}=\left[\mathbf{D}-\frac{1}{d}\mathbf{a}\mathbf{b}^{T}\right]\dot{\boldsymbol{\varepsilon}} \tag{4.30}$$

In general, this equation cannot be integrated analytically to obtain the resulting stresses for a given strain history, so that numerical procedures are needed. Here, a considerable number of numerical schemes are available, ranging from simple Euler forward-marching schemes to implicit schemes which take account of higher order derivatives. Especially for pressure-sensitive materials the choice of such an integration scheme is very critical and may significantly influence the results (Vermeer, 1980).

4.6 *Discussion of the perfectly-plastic model*

In order to avoid the angular form of the Coulomb yield surface, several approximations have been proposed. Certainly, the right circular cone of Drucker and Prager (1952) is the simplest option. Unfortunately, the circular cone approximates the Coulomb surface very poorly for higher friction angles, say $\phi \geqslant 30°$, which are found for sand and

concrete. For high friction angles we almost have a triangular cone (see Fig. 4.4.a), and a triangle certainly does not resemble a circle. The Drucker-Prager approximation is useful for soft clays with low friction angles but not for sand, rock or concrete. More accurate smooth surfaces have been proposed by Lade and Duncan (1975), and by Matsuoka and Nakai (1982). Recently Lade (1983) has also compared his criterion for concrete data. For a further discussion of smooth and angular yield surfaces the reader is referred to Section 7.4, where we will also briefly touch upon the so-called "tension cut-offs".

Obviously, the assumption of perfect plasticity is by far the most rigorous. It has been adopted merely as a first approximation to the behaviour of real granular materials, and this first approximation is useful mainly for three purposes:

- The calculation of limit loads: more sophisticated models generally cost more computer time, whilst the limit loads are not calculated much more accurately.
- The estimate of displacements and stresses in non-homogeneous soil and rock masses where we have relatively little data so that there is no point in the application of more sophisticated models.
- It is a good introduction into the behaviour of granular materials.

Another important idealization has tacitly been assumed. When choosing the Cartesian coordinate axes in the directions of the principal axes of stress, the model yields $\dot{\gamma}^{p}_{xy} = 0$ independently of the stress increments applied. The model has the property that the plastic strain rate is coaxial with the principal axes of stress. For non-rotating stress axes, as occur in most testing devices, this seems plausible, but it is not rational when the axes rotate. For a theoretical treatment of this subject the reader is referred to De Josselin de Jong (1971), to Rudnicki and Rice (1975) and to Vermeer (1981). Deviations from coaxiality have for instance been found in experiments on crushed glass, which have amongst other been carried out by Allersma (1982). Throughout this paper we adopt the idealization of coaxiality, as it facilitates the implementation and operation of plasticity models in finite element codes. Nevertheless, considering the increasing enhancement of numerical capabilities, we expect that non-coaxial models will become operational in the future.

5 Some consequences of non-associated plasticity

Numerical solutions of practical problems have already been shown in Figs. 2.2, 2.3 and 2.4. All the load-deflection curves have a small linear elastic portion and then a portion of decreasing slope. It depends on the particular problem whether or not a limit point is found where the load-deflection curve has a slope equal to zero. Limit points are, for instance, found for the indentation problems in the Figs. 2.2 and 2.3 but not for the dome structure in Fig. 2.4. The curves in Fig. 2.2 show a post-peak regime with some softening, but this is due to numerical inaccuracies. However, the use of the present model may well lead to real softening, that is, a negative slope of the load-deflection curve. We happened to find this behaviour when calculating load-displacement curves for simple-shear tests (e.g. Fig. 5.4). These tests are widely used for soil and currently

also in some research projects for concrete, for example by Sture (1983) and by Christensen and Willam (1983).

5.1 *Softening and hardening in isochoric simple-shear tests*

The shear-box test as depicted in Fig. 4.2 has fallen from favour as an instrument of fundamental research because it tends to give non-uniform stresses in the rupture zone (see for instance Christensen and Willam, 1983). In order to obtain uniform stresses, a so-called simple-shear apparatus was developed (Roscoe, 1953). A particular version of this device is shown in the insert to Fig. 5.1. Unfortunately, uniformity of stresses and strains is not generally achieved (Wood and Budhu, 1980), but we will assume an ideal test with full uniformity.

The apparatus in Fig. 5.1 is such that all normal strains can be kept equal to zero, so that we have a so-called isochoric test (no volume changes). We consider such a test for a sand with

$$E = 45 \text{ MPa}, \qquad \nu = 0.2, \qquad \phi = 43°, \qquad c = 0$$

These particular data follow from the experimental curves in Fig. 3.5. For the initial stress state in the specimen, we assume $\sigma_{yy} = -100$ kPa, $\sigma_{xx} = \sigma_{zz} = -25$ kPa and $\sigma_{xy} = 0$. During the test all strain rates vanish, with the exception of the shear-strain rate $\dot{\gamma}_{xy}$. So equation (4.14) simply gives

$$\dot{\sigma}_{xy} = \left(D_{33} - \frac{1}{d} a_3 b_3\right) \dot{\gamma}_{xy} \tag{5.1}$$

Numerical integration of this equation then results in the curves of Fig. 5.1. The upper curve is obtained for a dilatancy angle of 15°. Despite the use of a non-hardening model, this curve shows hardening. Indeed, the slope of the curve gradually decreases to reach a constant, but positive value. So elastic-perfectly plastic models do not necessarily

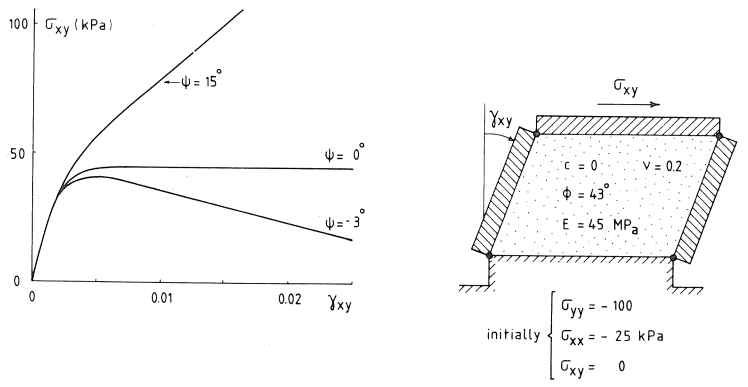

Fig. 5.1 Computed responses of sand in isochoric shear tests.

involve limit loads. Indeed, for the particular case of $\phi = \psi$, which is commonly referred to as associated plasticity in contrast to non-associated plasticity ($\phi \neq \psi$), we observe that there exists no limit load.

When using a negative dilatancy angle, we find the lower curve in Fig. 5.1. This stress-strain curve gradually approaches a line with a negative slope. In other words, hardening is followed by softening and during this unstable behaviour the shear resistance vanishes completely. Slightly negative dilatancy angles are characteristic of extremely loose sands as are found along some coastal lines of the Netherlands. The present constitutive model explains the sudden liquefaction phenomena as observed on some such coasts. The computed softening is somewhat surprising as the model is based on perfect plasticity, but we will see that this is a merit of non-associated plasticity.

In plasticity literature (for instance Drucker, 1952) softening behaviour is referred to as unstable. In fact, the equilibrium is unstable under dead load, and it would be more accurate to say "potentially unstable", but all softening is conveniently referred to as unstable. In order to arrive at a better understanding of the phenomenon, it is helpful to consider the stress path for the isochoric shear test by plotting the major and minor principal stresses (σ_1 and σ_3) in a stress plane. The stress path begins at the point A in Fig. 5.2 with $\sigma_1 = -100$ kPa and $\sigma_3 = -25$ kPa. Then the stresses are more or less controlled by the elastic volume change

$$\dot{\varepsilon}_v^e = \frac{E}{1-2\nu}(\dot{\sigma}_1 + \dot{\sigma}_2 + \dot{\sigma}_3) = E\frac{1+\nu}{1-2\nu}(\dot{\sigma}_1 + \dot{\sigma}_3) \tag{5.2}$$

The first identity follows from Hooke's law and the subsequent derivation is obtained by substituting the plane-strain condition $\dot{\sigma}_2 = \nu(\dot{\sigma}_1 + \dot{\sigma}_3)$. In the beginning of the test the strains are entirely elastic, so that the condition of zero volume strain implies

$$\dot{\varepsilon}_v^e = 0 \rightarrow \dot{\sigma}_1 + \dot{\sigma}_3 = 0 \tag{5.3}$$

This gives the elastic stress path A-B in Fig. 5.2.

The stress point B is on the yield locus for $f = 0$, and from this point on plastic strains

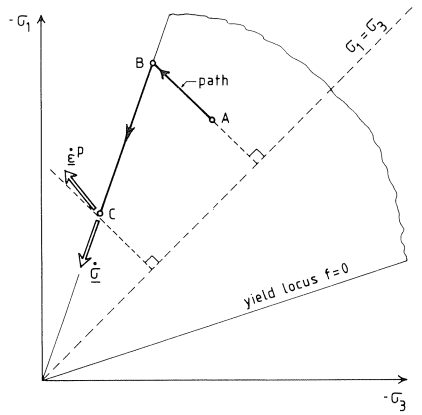

Fig. 5.2 The negativeness of $\dot{\boldsymbol{\sigma}}^T\dot{\boldsymbol{\varepsilon}}^p$ and $\dot{\boldsymbol{\sigma}}^T\dot{\boldsymbol{\varepsilon}}$ explains the unstable lower curve in Fig. 5.1.

develop, including plastic volume change when ψ is non-zero. Then an elastic volume change is needed to compensate for the plastic volume change. For a negative dilatancy angle, plastic contraction must be balanced by elastic expansion, or in formula

$$\dot{\varepsilon}_v^e = -\dot{\varepsilon}_v^p \rightarrow \dot{\sigma}_1 + \dot{\sigma}_3 > 0 \tag{5.4}$$

The elastic expansion gives rise to tensile stress increments, so that the existing compressive stresses will vanish. This is visualised by the stress path B-C in Fig. 5.2. Here, the stress-rate vector is tangent to the yield locus ($f = 0$) and points in the direction of the origin ($\dot{\sigma}_1 + \dot{\sigma}_3 > 0$). In Fig. 5.2 we have also plotted the plastic strain rate as a vector. Then it is seen that the plastic strain-rate vector forms an obtuse angle with the stress-rate vector. As a consequence the inner product is negative, or in formula

$$\dot{\boldsymbol{\sigma}}^T \dot{\boldsymbol{\varepsilon}}^p < 0 \tag{5.5}$$

This is the usual definition of unstable material behaviour. The negativeness of the above inner product is a necessary but not a sufficient condition for softening behaviour. For softening we need to consider the inner product of the stress rate and the total strain rate rather than the plastic strain rate. In Fig. 5.2 the total strain rate is always parallel to the line AB, making an obtuse angle to the stress-rate vector. Finally it is noted that softening is not only possible for $\psi < 0$ but more generally for $\psi < \phi$ as demonstrated in Fig. 5.4.

5.2 *Theoretical basis for $\psi < \phi$*

In the theory of associated plasticity, material stability is assured by Drucker's postulate, and unstable stress paths are excluded by assuming a plastic strain rate that is normal to the yield locus. For granular material this can be achieved by taking $\phi = \psi$, but this is not observed in triaxial testing and neither in shear testing (Roscoe, 1970). Furthermore, the idea is to be rejected from a theoretical viewpoint. We pursue the theoretical argument by considering the dissipated energy in a test, say a shear test on a material element of unit volume.

$$W = \int_0^t \boldsymbol{\sigma}^T \dot{\boldsymbol{\varepsilon}} \, dt \tag{5.6}$$

A theoretically sound model should be such that the dissipated energy is non-negative for any possible stress cycle of loading and reloading; otherwise the material would produce energy. For the model under consideration this implies a non-negative integrand.

For a cohesionless material we can show that

$$W \geqslant 0 \rightarrow \boldsymbol{\sigma}^T \dot{\boldsymbol{\varepsilon}} \geqslant 0 \rightarrow \phi \geqslant \psi \tag{5.7}$$

Rather than proving these inequalities in detail, we will demonstrate that there is no energy dissipation for $\phi = \psi$. The situation is visualised in Fig. 5.3 where the plastic strain rate is plotted normal to the yield locus of a cohesionless material. We then see that the plastic strain-rate vector is also normal to the total stress vector. Hence, the

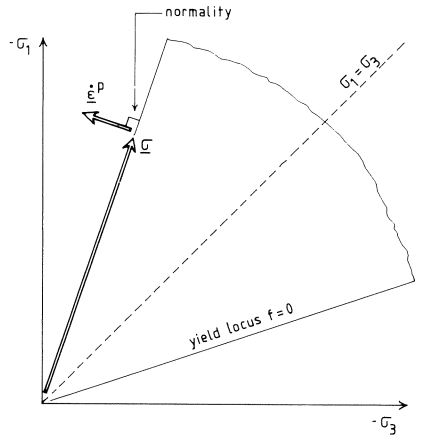

Fig. 5.3 For cohesionless material the flow cannot be normal to the yield surface as the plastic work would vanish.

inner product of these vectors vanishes so that there is no energy dissipation ($\dot{W} = 0$) when normality holds. As plastic deformation without energy dissiplation is inconceivable and we are forced to abandon associated plasticity.

5.3 *Non-uniqueness of the limit load*

In the foregoing we have seen that a load-deflection curve may involve a limit load. In associated plasticity a limit load is unique in that the value does not depend on the initial stresses before loading nor on the sequence in which different load components are applied. In non-associated plasticity, however, the limit load may be influenced by initial stresses and the sequence of loading. In order to demonstrate this influence we consider the simple-shear test again, but this time we allow volume changes.

First consider a specimen in an initial state "A" with specifications

A: $\sigma_{yy} = -100$ kPa, $\sigma_{xx} = \sigma_{zz} = -25$ kPa, $\sigma_{xy} = 0$

This state of stress coincides with the initial stresses of the isochoric test treated earlier in this chapter. The material constants are also assigned the same values as in the isochoric shear test. In the standard (simple) shear test considered now, the specimen is sheared at a constant vertical stress of -100 kPa. On simulating this test in a computer run, we find the curve A of Fig. 5.4. Curve B represents results of a computer run for a specimen with the same constant vertical stress but a much higher initial horizontal stress, viz. -400 instead of -25:

B: $\sigma_{yy} = -100$ kPa, $\sigma_{xx} = \sigma_{zz} = -400$ kPa, $\sigma_{xy} = 0$

These initial stresses give a marked peak in the load-deflection curve with a high limit load (or peak strength). By carrying out a whole series of computations for different

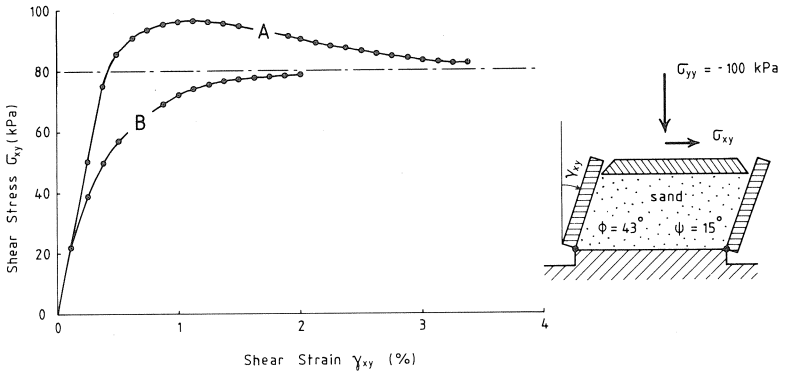

Fig. 5.4 Computed responses of sand in simple shear; the limit load depends on the initial stresses.

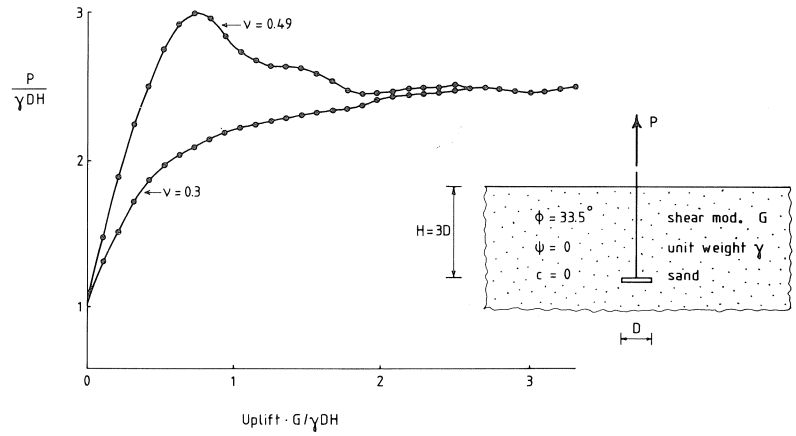

Fig. 5.5 Finite element results for an anchor in sand; the limit load depends on Poisson's ratio.

initial horizontal stresses, different limit loads are found. On the other hand, the residual strength is found to be the same.

The influence of the initial stresses is also relevant to practical engineering problems. An illustrative example is the anchor problem as schematized in the insert to Fig. 5.5. Again, the non-hardening Coulomb model was used to compute the load-carrying capacity of the anchor (Vermeer and Sutjiadi, 1985). Similarly to the standard shear test, different initial stresses show different limit loads, but again a unique residual load is found. As the initial stresses are seldom known precisely, such anchors should be designed for the residual load and not for a peak strength that happens to be found for a particular assumption as to the initial state of stress. Fig. 5.6 shows a measured load-deflection curve for an anchor that involves a marked peak. It is a typical response of an embedded structure. Many computer programs cannot simulate the unstable post-peak

behaviour and then the computations are stopped slightly prior to the limit load. The present examples show that there is a need for computations beyond the limit load down to a possibly lower residual load. For small-deformation problems in associated plasticity, softening is precluded and the limit load simply coincides with the residual load. Then there is less need for calculations in the fully plastic range.

5.4 Geometric destabilization and stabilization

The measured data in Fig. 5.6 show continuing destabilization (or softening), whereas the computed curves in Fig. 5.5 have a constant residual load. This is because geometry changes are neglected in the computations. When an embedded anchor is pulled, the anchor depth diminishes so that the load-carrying capacity decreases and it vanishes when the anchor reaches the soil surface. This effect produces the linear softening in the measurements of Fig. 5.6. It is referred to as a geometric destabilization as it is a consequence of geometry changes. It is also possible that geometry changes invoke a stabilization instead of a destabilization. An example of such a problem is the foundation

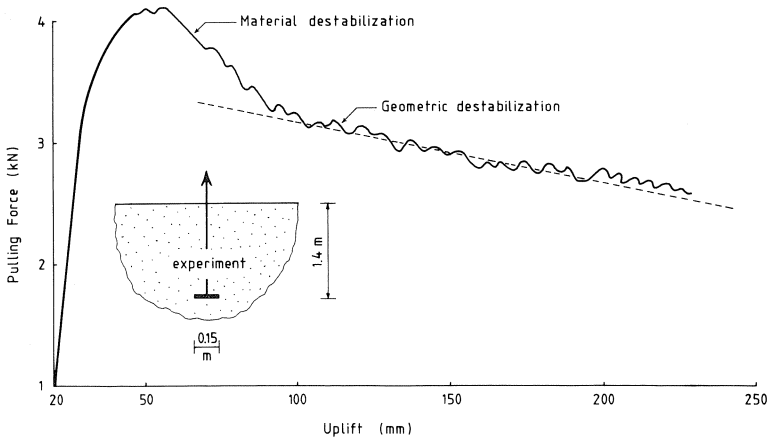

Fig. 5.6 Experimental results for an anchor in sand.

plate on soil. When a non-tilting plate is thrust by punching into a soil bed, the measured load deflection-curve will not show a limit load but continued hardening. The load-carrying capacity increases with deformation due to the upheave of the adjacent soil surface and the increasing embedment of the plate. The computational results in Figs. 2.2 and 2.3 do not show this as geometry changes are neglected in the conventional small-deformation analysis that is used for all the computations in this paper.

6 Concepts of isotropic hardening

The non-hardening model is very useful for failure problems, as limit loads and residual loads can be computed quite accurately. On the other hand, perfect plasticity is less suit-

able for the study of the development of displacements under working loads, because this type of model involves a considerable overestimation of the elastic range. For this application hardening plasticity is much more suitable.

From a theoretical viewpoint, the theory of hardening plasticity is not much different from perfect-plasticity theory. Again, the strain rate is divided into two additive contributions. The elastic component occurs for all changes of stress and the plastic component may occur when the stresses satisfy the yield condition $f = 0$. Hence, similar to a non-hardening model, a hardening model involves the equations

$$\dot{\boldsymbol{\varepsilon}} = \dot{\boldsymbol{\varepsilon}}^{\mathrm{e}} + \dot{\boldsymbol{\varepsilon}}^{\mathrm{p}}$$

$$\dot{\boldsymbol{\varepsilon}}^{\mathrm{e}} = \mathbb{D}^{-1}\dot{\boldsymbol{\sigma}}$$

$$\dot{\boldsymbol{\varepsilon}}^{\mathrm{p}} = \lambda \frac{\partial g}{\partial \boldsymbol{\sigma}}$$

The multiplier λ vanishes for stress variations in the elastic range $f < 0$ and for unloading $\dot{f} < 0$. The difference from the theory of perfect plasticity relates to the size of the elastic range and thus to the yield function f. The difference is represented in Fig. 6.1. In hardening plasticity the elastic range depends on the plastic strain of the material element considered and we speak of isotropic hardening when an initially small elastic range expands as a functional of the plastic deformation, but when the centre of the

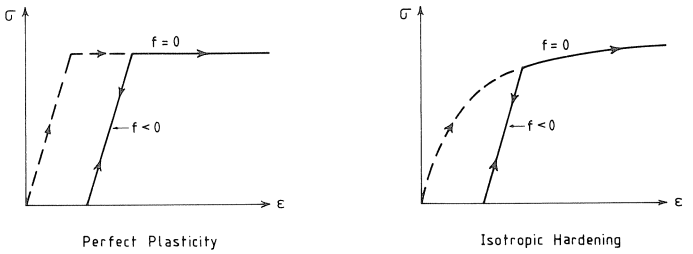

Fig. 6.1 For isotropic hardening, the elastic range expands with increase of plastic deformation.

yield surface does not change during the loading process. As a consequence, some plastic strain measure must enter into the yield function f. The yield condition must be of the form

$$f(\sigma_1, \sigma_2, \sigma_3, \varkappa) = 0 \tag{6.1}$$

at least for isotropic hardening as considered in this section. The scalar parameter $\varkappa$ is some functional of the plastic strain history, and is usually named a hardening parameter. When using such a yield function it can be shown that there are no orientation effects in a stress free material, so that the material remains isotropic.

6.1 *The hardening parameter*

A simple example of a possible definition for a hardening parameter is the volumetric plastic strain

$$\varepsilon_v^p = \varepsilon_1^p + \varepsilon_2^p + \varepsilon_3^p \tag{6.2}$$

This particular choice is useful for a highly compressible material like clay (Schofield and Wroth, 1968). In general the elastic range will depend not only on the current plastic strain, but on the plastic strain history as well: the elastic range is said to be a functional of the plastic strain rather than a function of the plastic strain. Obviously, this could lead to a complicated theory, but this is avoided by assuming that the plastic strain history can also be captured in the hardening parameter. In metal plasticity this is done by the hardening parameter (Hill, 1950).

$$\bar{\varepsilon}^p = \int \sqrt{\left(\tfrac{2}{3}\dot{\boldsymbol{\varepsilon}}^{pT}\dot{\boldsymbol{\varepsilon}}^p\right)}\, dt \tag{6.3}$$

or in terms of principal strain rates

$$\bar{\varepsilon}^p = \int \sqrt{\left\{\tfrac{2}{3}\left(\dot{\varepsilon}_1^p\dot{\varepsilon}_1^p + \dot{\varepsilon}_2^p\dot{\varepsilon}_2^p + \dot{\varepsilon}_3^p\dot{\varepsilon}_3^p\right)\right\}}\, dt \tag{6.4}$$

The factor $\frac{2}{3}$ is convenient for the evaluation of uniaxial tests. In stressing a metal bar we have

$$\varepsilon_2^p = \varepsilon_3^p = -0.5\varepsilon_1^p \qquad \text{(uniaxial test with } \varepsilon_v^p = 0)$$

as metals show no plastic volume change. Then the so-called effective strain, $\bar{\varepsilon}^p$, simply coincides with the uniaxial plastic strain.

$$\bar{\varepsilon}^p = |\varepsilon_1^p| \qquad \text{(uniaxial test with } \varepsilon_v^p = 0)$$

Instead of the effective strain integral, a plastic work integral is sometimes employed. The plastic work that is done in a deformation process is

$$W^p = \int \boldsymbol{\sigma}^T\dot{\boldsymbol{\varepsilon}}^p\, dt \tag{6.5}$$

In metal plasticity it is quite possible to make use of the plastic work, as it leads to a model which is entirely equivalent to a model that employs the effective strain. Indeed, for the Von Mises yield function for metals, both definitions yield exactly the same results. Some recent models for soils are also based on the concept of plastic work, but we will show that for granular materials (both non-cemented and cemented), the effective strain is much more suitable and not equivalent to the plastic work. Further, many experiments were performed on sand specimens for the purpose of assessing the best definition of the hardening parameter. Both Stroud (1971) and Tatsuoka and Ishihara (1975) reported evidences for quantities that resemble the effective strain very closely. Therefore, the derivations in the following will be based on a parameter which is either exactly or approximately equal to the effective strain.

6.2 *Friction hardening for sand*

Fig. 6.2 shows the results of two triaxial tests on a dense sand. These responses are typical, as an initially stiff response is followed by a flat peak in the shear stress-axial strain curve. The peak strength increases almost linearly with the radial stress σ_3. In order to obtain a unique curve for all tests, the shear stress must be replaced by the principal stress ratio σ_1/σ_3 as was done in Fig. 3.5. Indeed, the stress ratio-axial plastic strain curve appears to be unique for all compression tests with various axial stresses. Hence, there exists a relationship of the form

$$f(\sigma_1/\sigma_3, \varepsilon_1^p) = 0 \qquad \text{for } \sigma_3\text{-constant tests} \tag{6.6}$$

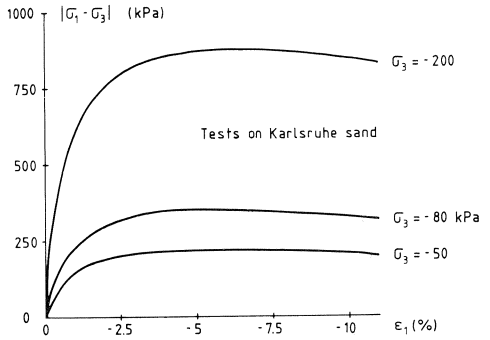

Fig. 6.2 Replot of sand data after Hettler and Vardoulakis (1984).

Restriction must be made to increasing stress ratios as unloading and reloading show a different more or less elastic response. The use of the principal stress ratio is not strictly necessary. In fact, we may also use the stress measures τ^* and σ^* as previously used in the yield function of the non-hardening model.

$$\sigma_1 = -(\sigma^* + \tau^*), \qquad \sigma_3 = -\sigma^* + \tau^*, \qquad \sigma_1/\sigma_3 = (\sigma^* + \tau^*)/(\sigma^* - \tau^*)$$

This implies that τ^*/σ^* instead of σ_1/σ_3 may be used in a yield condition of the form $f(\tau^*/\sigma^*, \varepsilon_1^p) = 0$.

In order to include other tests in addition to the common σ_3-constant tests, the axial strain must be replaced by the more general effective strain $\bar{\varepsilon}^p$. Replacing ε_1^p by $\bar{\varepsilon}^p$ the condition $f(\tau^*/\sigma^*, \bar{\varepsilon}^p) = 0$ follows. In the following we will use the equivalent condition

$$f = \tau^* - \sigma^* \sin \phi^* = 0 \quad \text{or} \quad \tau^* = \sigma^* \sin \phi^* \tag{6.7}$$

where $\sin \phi^*$ is some function of the effective strain. This notation of the yield condition is chosen because it resembles the non-hardening yield condition (4.7) very closely. Instead of a constant friction angle ϕ, we now use a strain-dependent quantity ϕ^* that will be referred to as the mobilised friction angle. Experience shows that the experi-

mental curves from sand testing can usually be expressed in a simple form, e.g. the relationship

$$\sin \phi^* = 2 \frac{\sqrt{(\bar{\varepsilon}^p \varepsilon^f)}}{\bar{\varepsilon}^p + \varepsilon^f} \sin \phi \qquad \text{for } \bar{\varepsilon}^p < \varepsilon^f$$

$$\sin \phi^* = \sin \phi \qquad \text{for } \bar{\varepsilon}^p > \varepsilon^f \tag{6.8}$$

so that the mobilised friction angle gradually increases with strain to reach the limit friction angle when $\bar{\varepsilon}^p$ has reached the constant ε^f. Other useful formulas are given by Brinch Hansen (1965).

For an uncemented granular material, the concept of friction hardening is quite rational. Consider for instance an assembly of particles in static equilibrium under a vertical load intensity of σ_1 and a horizontal load intensity σ_3. Furthermore, let the particles be rigid and unbreakable. Then a proportional increase of σ_1 and σ_3 will cause a proportional increase of the interparticle forces at the contact points between the particles, so that the directions of the contact forces are not changed. On the other hand, a change of the ratio σ_1/σ_3 will change the direction of the contact forces and will result in slip at a number of contact points. The occurrence of interparticle slip implies a rearrangement of the particles, that is plastic deformation in a macroscopic sense. Thus, the plastic deformation is related to the stress ratio alone, as formulated by the above yield function and confirmed by the test data in Fig. 3.5. Here, it should be noted that the test data in Figs. 3.5 and 6.2 were obtained for a pure quartz sand with very hard and strong particles. Other sands have softer particles with breakable edges, in which case the test data are not entirely matched by pure friction hardening. The yield function must then be modified by making ϕ^* also a function of a stress level measure such as σ^*. For details the reader is referred to Vermeer (1984).

6.3 *Friction hardening versus cohesion hardening*

Obviously, the above yield condition cannot be applied to concrete or rock in a straightforward manner as it incorporates no cohesive strength. For such cohesive materials, the yield condition could be extended to

$$\tau^* = \sigma^* \sin \phi^* + c \cos \phi^* \tag{6.11}$$

When ϕ^* has increased up to ϕ, this formulation gives the yield condition (4.10) as previously used in the non-hardening model. However, this is not the only possibility for modelling concrete behaviour, and a different yield condition will be considered in the following.

Isotropic hardening models were initially developed for the study of metals, with yield conditions of the form

$$\tau^* = c^*, \quad c^* = c^0 + h\bar{\varepsilon}^p \qquad \text{(for metals)} \tag{6.12}$$

or non-linear relations between c^* and $\bar{\varepsilon}^p$ with constants similar to c^0 and h. This type

of hardening (for $h > 0$) may be referred to a cohesion hardening because the cohesion increases as a function of the effective strain. Note that many authors on metal plasticity employ the yield stress in uniaxial tension rather than the mobilised cohesion c^*, but this is not important as the uniaxial yield stress is twice the mobilised cohesion. The concept of cohesion hardening could also be extended to include friction and this would lead to a yield condition like

$$\tau^* = \sigma^* \sin \phi + c^* \cos \phi \tag{6.13}$$

Mathematically there is little difference from the friction hardening formulation (6.11), but cohesion hardening gives entirely different stress-strain curves as illustrated in Fig. 6.3. For friction hardening different triaxial compression tests have the same elastic range, whereas this range increases with the radial stress σ_3 in the case of cohesion hardening. The hardening range in Fig. 6.3a is determined by relation (6.10) between $\sin \phi^*$ and $\bar{\varepsilon}^p$, and a similar non-linear relationship between c^* and $\bar{\varepsilon}^p$ is used in Fig. 6.3b. Experimental data as plotted in Fig. 3.7 indicate that concrete behaviour is much better fitted by friction hardening than by cohesion hardening. Therefore, pure

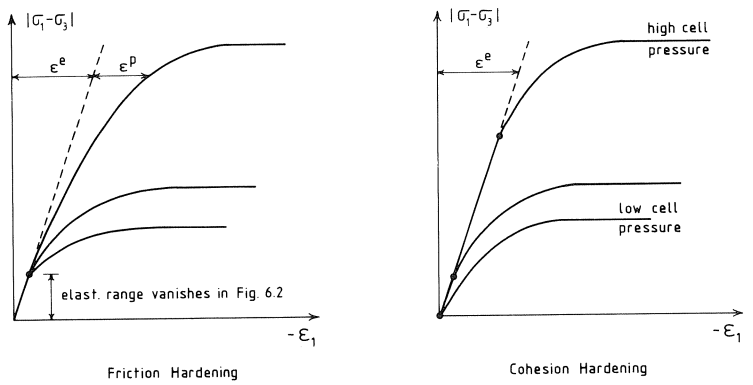

Fig. 6.3 Friction hardening differs from cohesion hardening in the size of the elastic range.

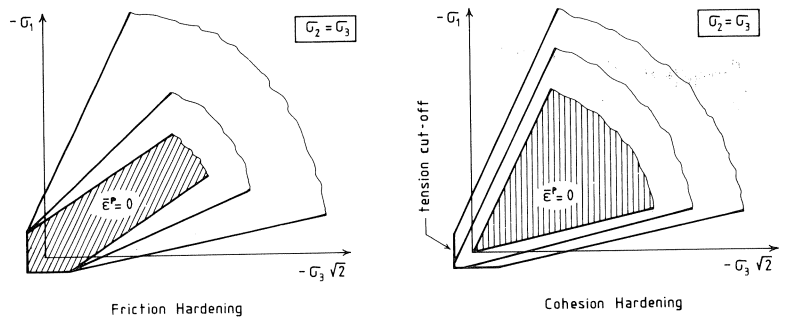

Fig. 6.4 Largely different modes of expansion for the elastic range.

cohesion hardening is not attractive and recent trends in modelling concrete behaviour employ a form of friction hardening (see for instance Schreyer, 1983). The difference between friction hardening and cohesion hardening is most clearly reflected by the expansion of the yield surface in the stress space. Fig. 6.4a shows successive positions of the yield surface when using the condition (6.11) whilst Fig. 6.4b corresponds to equation (6.13).

In order to demonstrate that we have several slightly different versions of friction hardening rather than one unique form, we give

$$\tau^* = (\sigma^* + c \operatorname{cotan} \phi) \sin \phi^* \tag{6.14}$$

as an alternative for the yield condition (6.11). The difference between both formulations for friction hardening is illustrated in Fig. 6.5. The question of the best formulation is still open; it must be answered by considering a great deal of empirical data.

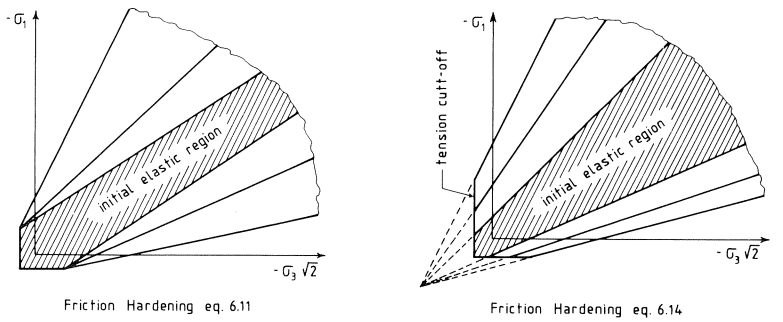

Fig. 6.5 Alternatives within friction hardening.

7 A hardening-softening model unifying granular materials

In this chapter we will attempt to give a unified treatment of loose and of cemented granular materials. This will be done within the framework of isotropic hardening and softening. Rather than modelling all subtleties of the material behaviour, we will concentrate on the main features as observed in monotonic loading.

7.1 *The yield function*

In the preceding chapter, friction hardening was found to be important for loose as well as for cemented granular materials, i.e. the mobilised friction angle increases as a function of the effective strain. It is also obvious that, for a proper description of cemented materials, the yield function must take account of the cohesive strength. Just as for the mobilised friction angle ϕ^*, we introduce a mobilised cohesion c^* in the yield function f

$$f = \tau^* - \sigma^* \sin \phi^* - c^* \tag{7.1}$$

$$\sin \phi^* = 2 \frac{\sqrt{(\bar{\varepsilon}^p \varepsilon^f)}}{\bar{\varepsilon}^p + \varepsilon^f} \sin \phi$$

where the equation for the mobilised friction angle is similar to the one introduced in the preceding chapter, and is only repeated here for the sake of self-sufficiency of this chapter. The reader may also note that the yield function (7.1) differs only marginally from the friction hardening formulation (6.11); the term $c \cos \phi^*$ is simply replaced by c^*.

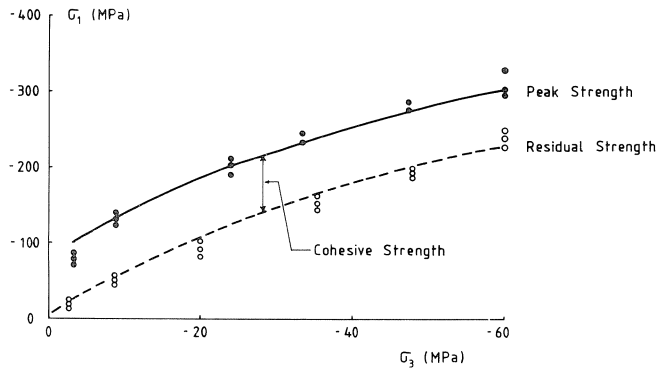

Fig. 7.1 Triaxial test results for sandstone after Kovari (1977); the cohesive strength vanishes due to micro-cracking.

Some idea of the $c^* - \bar{\varepsilon}^p$ relation is given by Fig. 7.1, which present test results on a sandstone. We observe a considerable difference between the peak strength and the residual strength, the difference being approximately equal to the cohesion. Other test results indicate that the difference between the two strengths tends to vanish when the confining pressure increases. These phenomena could be modelled by applying softening on the cohesion. A possible choice for the $c^* - \bar{\varepsilon}^p$ relation is:

$$c^* = c \exp \left[- \left(\frac{\bar{\varepsilon}^p}{\varepsilon^c} \right)^2 \right] \tag{7.2}$$

where ε^c is a constant similar to ε^f in de hardening relation (6.8) for the mobilised friction angle ϕ^*. Both the softening relation for c^* and the hardening relation for ϕ^* are plotted in Fig. 7.2. The softening on the cohesion can be made plausible by considering that when a specimen of intact rock or concrete is sheared, micro-cracks first develop, and that at failure the specimen is heavily cracked. Hence, the cementation of the material gradually decreases so that also the cohesive strength of the material vanishes. Accordingly, the initially cemented material will become more similar to a particulate material with only friction hardening. The performance of the model is demonstrated in Fig. 7.3. This figure gives only an impression of the possibilities of the model, but no attempt has been made to fit any existing data accurately. Nevertheless, the increased ductility with increasing confining pressure is modelled.

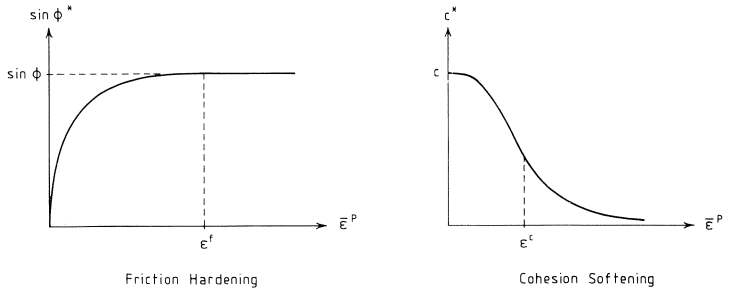

Fig. 7.2 Quasi-empirical relations in the hardening-softening model.

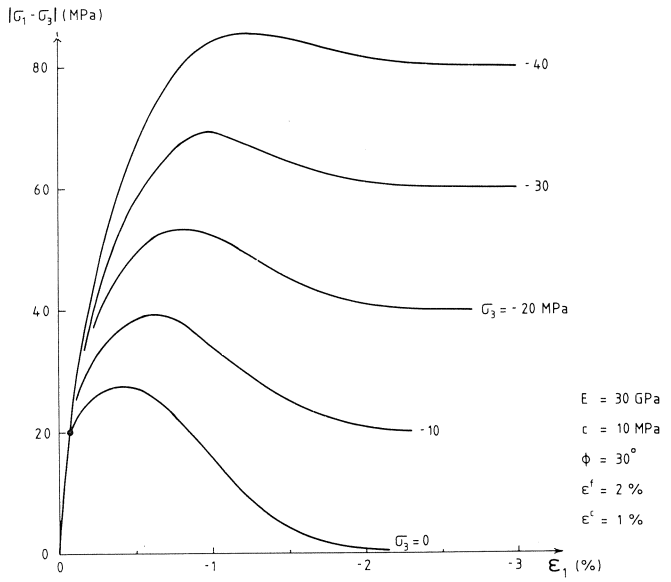

Fig. 7.3 Computed responses of a cemented material in triaxial tests.

7.2 *Plastic potential and row flow rule*

For the hardening model, and also for the hardening-softening model developed in this chapter, we use again a plastic potential function which is almost identical with the yield function, namely

$$g = \tau^* - \sigma^* \sin \psi^* + \text{constant} \tag{7.3}$$

For $\psi^* = \phi^*$ this function would coincide with the yield function (7.1) and we would arrive at an associated model. Like the perfectly plastic model, the hardening model is formulated in the spirit of Coulomb and Tresca by using an angular yield surface and an angular plastic potential surface in the principal stress space (Figs. 4.3 and 4.4). As also discussed in Chapter 4 for the perfectly-plastic model, the derivation of the flow rule

from the potential function resolves itself into two procedures, one for stress points at the corners and the other for stress points at the flat sides with $\sigma_1 < \sigma_2 < \sigma_3$. For brevity, we will only consider the latter case.

When the intermediate principal stress does not coincide with the major or minor principal stress, the plastic potential function is differentiable and we have the usual flow rule

$$\dot{\boldsymbol{\varepsilon}}^{\mathrm{p}} = \lambda \frac{\partial g}{\partial \boldsymbol{\sigma}}$$

In terms of principal strain rates this gives

$$\begin{aligned} \dot{\varepsilon}_1^{\mathrm{p}} &= \lambda \frac{\partial g}{\partial \sigma_1} = -\tfrac{1}{2}\lambda(1 - \sin \psi^*) \\ \dot{\varepsilon}_2^{\mathrm{p}} &= \lambda \frac{\partial g}{\partial \sigma_2} = 0 \\ \dot{\varepsilon}_3^{\mathrm{p}} &= \lambda \frac{\partial g}{\partial \sigma_3} = \tfrac{1}{2}\lambda(1 + \sin \psi^*) \end{aligned} \tag{7.4}$$

In analogy with the mobilised friction angle ϕ^*, we have now introduced a mobilised dilatancy angle ψ^*. We retrieve the flow rule for the perfectly-plastic model by setting $\psi^* = \psi$. For the present model, a constant dilatancy angle is not sufficient, and we will need some stress-dilatancy relation, which will be discussed in a subsequent section. Equation (6.3) may now be used to derive that

$$\dot{\bar{\varepsilon}}^{\mathrm{p}} = \lambda \sqrt{[\tfrac{1}{3}(1 + \sin \phi^* \sin \psi^*)]}$$

This relationship with the effective strain is important because it allows further calculation of the multiplier λ. For this calculation we also use the consistency equation

$$\dot{f} = \frac{\partial f^{\mathrm{T}}}{\partial \boldsymbol{\sigma}} \dot{\boldsymbol{\sigma}} + \frac{\partial f^{\mathrm{T}}}{\partial \bar{\varepsilon}^{\mathrm{p}}} \dot{\bar{\varepsilon}}^{\mathrm{p}} = 0$$

The combination of the two equation gives

$$\lambda = \frac{1}{h} \frac{\partial f^{\mathrm{T}}}{\partial \boldsymbol{\sigma}} \dot{\boldsymbol{\sigma}} \tag{7.5a}$$

$$h = -\sqrt{[\tfrac{1}{3}(1 + \sin \phi^* \sin \psi^*)]} \frac{\partial f}{\partial \bar{\varepsilon}^{\mathrm{p}}} \tag{7.5b}$$

In fact, the influence of the (mobilised) dilatancy angle on the hardening modulus h is negligible. Consider for instance an extremely large dilatancy angle of 20° and a friction angle of 35°. Then we have $\sqrt{(1 + \sin \phi^* \sin \psi^*)} = 1.094$ which means that the influence of the dilatancy angle upon the hardening modulus is at most 9.4%.

Substituting the expression for λ in the flow rule (7.4) and adding elastic strain rates, we obtain

$$\dot{\boldsymbol{\varepsilon}} = \dot{\boldsymbol{\varepsilon}}^{\mathrm{e}} + \dot{\boldsymbol{\varepsilon}}^{\mathrm{p}} = \mathbf{D}^{-1}\dot{\boldsymbol{\sigma}} + \frac{1}{h}\frac{\partial g}{\partial \boldsymbol{\sigma}}\frac{\partial f}{\partial \boldsymbol{\sigma}}^{\mathrm{T}}\dot{\boldsymbol{\sigma}} \tag{7.6a}$$

or in inverse form

$$\dot{\boldsymbol{\sigma}} = \left[\mathbf{D} - \frac{\mathbf{D}\dfrac{\partial g}{\partial \boldsymbol{\sigma}}^{\mathrm{T}}\dfrac{\partial f}{\partial \boldsymbol{\sigma}}\mathbf{D}}{h + \dfrac{\partial f}{\partial \boldsymbol{\sigma}}^{\mathrm{T}}\mathbf{D}\dfrac{\partial g}{\partial \boldsymbol{\sigma}}}\right]\dot{\boldsymbol{\varepsilon}} \tag{7.6b}$$

The first form can be integrated when the stress path is given and the second form must be used when the stresses have to be computed for a given strain path.

7.3 *The hardening modulus h*

The hardening modulus governs the plastic strain rates in the same way as Young's modulus governs the elastic strain rates. We can demonstrate this by considering a compression test with both σ_2 and σ_3 being constant. Then we have

$$\dot{\varepsilon}_1 = \frac{1}{E}\dot{\sigma}_1 + \frac{1}{h}\frac{\partial g}{\partial \sigma_1}\frac{\partial f}{\partial \sigma_1}\dot{\sigma}_1$$

or after elaboration

$$\dot{\varepsilon}_1 = \frac{1}{E}\dot{\sigma}_1 + \frac{1}{h}(1 - \sin\psi^*)(1 - \sin\phi^*)\dot{\sigma}_1$$

In the special case of non-granular materials the angles of friction and dilatancy vanish and we obtain $\dot{\varepsilon}_1 = \dot{\sigma}_1/E + \dot{\sigma}_1/h$, which illustrates the analogy beween E and h. For granular materials, the involvement of the angles of dilatancy and friction make the situation more complicated, but it will be clear that the slope of a stress-strain curve is largely determined by the hardening modulus.

The hardening modulus increases almost linearly with the stress measure σ^*. It follows from equation (7.5b) and the yield function (7.1) that

$$h\sqrt{3} \approx -\frac{\partial f}{\partial \bar{\varepsilon}^{\mathrm{p}}} = \sigma^*\frac{\partial \sin\phi^*}{\partial \bar{\varepsilon}^{\mathrm{p}}} + \frac{\partial c^*}{\partial \bar{\varepsilon}^{\mathrm{p}}}$$

Indeed, the hardening modulus becomes truly proportional to σ^* when the mobilised cohesion vanishes or in the case where c^* is assumed to be a constant. The hardening modulus depends even more closely on the empirical relations for $\sin\phi^*$ versus $\bar{\varepsilon}^{\mathrm{p}}$ and c^* versus $\bar{\varepsilon}^{\mathrm{p}}$. The equations (6.8) and (7.2) that we proposed are such that the hardening modulus decreases dramatically with plastic strain increase. In Fig. 7.1 this is reflected by decreasing slopes of the stress-strain curves.

7.4 *The mobilised dilatancy angle*

In the foregoing we have defined a yield function including particular relations for

the mobilised friction angle ϕ^* and the mobilised cohesion c^*. On the other hand, the plastic potential function was introduced without specifying a precise relation between ψ^* and $\bar{\varepsilon}^p$. In this section the model will be completed by adding such a relationship.

The physical meaning of the mobilised dilatancy angle ψ^* is identical with the meaning of the (limit) dilatancy angle ψ which was used in the non-hardening model, namely

$$\sin \psi^* = \frac{\dot{\varepsilon}_1^p + \dot{\varepsilon}_3^p}{-\dot{\varepsilon}_1^p + \dot{\varepsilon}_3^p} \quad \text{for} \quad \sigma_1 < \sigma_2 < \sigma_3$$

This equation follows from the flow rule (7.4) and must be regarded as a definition. For the Coulomb type model considered here, the situation $\sigma_1 < \sigma_2 < \sigma_3$ implies $\dot{\varepsilon}_2^p = 0$ so that we may also write

$$\sin \psi^* = \frac{\dot{\varepsilon}_v^p}{-2\dot{\varepsilon}_1^p + \dot{\varepsilon}_v^p} \qquad \sigma_1 < \sigma_2 < \sigma_3 \text{ and } \sigma_1 < \sigma_2 = \sigma_3 \tag{7.7}$$

We prefer the latter notation as it can also be used in the case of common triaxial compression tests when $\sigma_1 < \sigma_2 = \sigma_3$ (see Section 4.4.). Note that σ_1 is the major compressive stress; it is negative, as tension is treated as positive. Test results as plotted in Figs. 3.5, 3.6 and 3.7 show a gradual increase of the dilation rate $-\dot{\varepsilon}_v^p/\dot{\varepsilon}_1^p$ up to a limit value at peak stress states. As a consequence, the mobilised dilatancy angle ψ^* gradually increases to a limit dilatancy angle ψ, which was used in the non-hardening model.

The gradual increase of the mobilised dilatancy angle will be modelled by adopting a relationship between ψ^* and the effective strain $\bar{\varepsilon}^p$. In soil mechanics the most popular approach has been to relate the dilation rate $-\dot{\varepsilon}_v^p/\dot{\varepsilon}_1^p$ to a stress ratio like σ_1/σ_3 or equivalently to the mobilised friction angle. Several more or less theoretical relations have been proposed. Roscoe et al. (1963) proposed a single-parameter equation on the basis of energy considerations. Another single-parameter equation was put forward by Rowe (1971), namely

$$1 - \dot{\varepsilon}_v^p/\dot{\varepsilon}_1^p = \left\{\frac{\tan (45° + \phi^*/2)}{\tan (45° + \phi_{cv}/2)}\right\}^2 \tag{7.8}$$

where ϕ_{cv} is a constant. It is referred to as the "friction angle of constant volume". This name is logical as the above mentioned equation gives $\dot{\varepsilon}_v^p = 0$ for $\phi^* = \phi_{cv}$. In fact, the equation predicts negative dilation for small angles of mobilised friction ($\phi^* < \phi_{cv}$) and positive dilation for larger values of this angle ($\phi^* > \phi_{cv}$). The constant marks a smooth turning point where plastic contraction stops and dilation begins. For sand the above equation was validated by several researchers, e.g. Stroud (1971) and Vermeer (1978), including the plastic contraction at the beginning of loading. For loose granular materials this contraction is plausible; the contraction is associated with plastic deformation due to the rearrangements of individual particles, whereas positive dilatation is associated with continued plastic deformation due to sliding between groups of particles. On the other hand, we may not expect plastic contraction when loading a solid concrete or non-porous rocks, because there are no voids that can be filled with material. For

such solid materials the above equation seems useful only in the range $\phi^* > \phi_{cv}$ where positive dilation is predicted.

We will use Rowe's so-called stress-dilatancy equation (7.8) as it is simple and accurate; it has been proved that it is accurate for sand whilst we expect reasonable accuracy for concrete and rock. However, we will conveniently use the equation in a different form. Eliminating $\dot{\varepsilon}_v^p/\dot{\varepsilon}_1^p$ from the equation (7.7) and (7.8), we obtain the more suitable form

$$\sin \psi^* = \frac{\sin \phi^* - \sin \phi_{cv}}{1 - \sin \phi^* \sin \phi_{cv}} \tag{7.9}$$

This is the desired relationship between the mobilised dilatancy angle and the effective strain as ϕ^* is a function of $\bar{\varepsilon}^p$. The mobilised dilatancy angle is initially negative and increases with increase of ϕ^*, i.e. when the effective strain increases. The negative values must not be used for solid materials; instead $\psi^* = 0°$ can be useful for $\phi^* < \phi_{cv}$. The constant ϕ_{cv} is readily calculated from the limit dilatancy angle ψ and the limit friction angle ϕ. By substituting $\phi^* = \phi$ and $\psi^* = \psi$ and rearranging equation (7.9) we obtain

$$\sin \phi_{cv} = \frac{\sin \phi - \sin \psi}{1 - \sin \phi \sin \psi} \tag{7.10}$$

From the concrete data in Fig. 3.7 we can derive $\phi = 35°$, $\psi = 12{,}6°$ and consequently $\phi_{cv} = 24°$ by means of the above equation. This is slightly below the range $25° < \phi < 33°$ that we know for quartz sands.

7.5 *Discussion of the model*

Sand, rock and concrete are complex materials and their mechanical behaviour is certainly not completely described by the idealization of isotropic hardening and softening. However, this idealization strikes a balance between accuracy and simplicity. Due to this combination, isotropic hardening is potentially capable of giving the engineer a true understanding of material behaviour. That merit is lost when complex functions are used in the formulation of the actual model. It is mainly for this reason that we use the Coulomb yield surface and a plastic potential of similar form. Other useful yield surfaces exist. A resembling smooth yield surface was for instance used in a so-called double hardening model (Vermeer, 1984). Lade (1983) and Schreyer and Babcock (1984) employ another function for the yield surface of concrete. Other options are for instance given by Willam and Warnke (1974) and by Chen (1982). However, the particular choice of a yield surface does not affect the basic ideas outlined here.

For plane strain situations the implementation of the model in a computer program is straightforward, but a special subroutine is needed for treating stress states at the apex of the yield cone. In fact, it is worthwhile to implement a subroutine that can treat any corner in a yield surface. Such a subroutine is also needed when we consider axisymmetric or general three-dimensional problems, due to the occurrence of ridges in the

yield surface. Ridges (common corners) are also introduced when tension cut-offs are introduced. For cohesive-frictional materials the apex of the Coulomb surface is usually cut off because a mere Coulomb yield condition would permit too large tensile stresses. Such a so-called tension cut-off also causes a singularity at the intersection with the Coulomb surface.

If follows from the above considerations that the model must be extended to include tension cut-offs when the material is cohesive. Obviously, the importance of this extension grows with increasing initial cohesion c. The significance of other extensions depends on the porosity of the material. Consider for instance a specimen of sand that is loaded hydrostatically. Then we may expect some densification, i.e. plastic volume contraction due to isotropic stressing. Indeed, loose sands show high densification and dense sands show moderate plastic volume changes approximately of the same magnitude as the elastic volume changes. Porous rocks display the same phenomenon, especially when the pressure exceeds a threshold value beyond which the interparticle bonds begin to collapse. Concrete is usually not very porous but even then the phenomenon is noticeable. The plastic volume change under hydrostatic load is not captured by the Coulomb yield surface as it is open in the direction of hydrostatic pressure. In order to capture the phenomenon, we need a yield cap that closes the Coulomb surface. Again, this extension gives a yield corner at the intersection of the two surfaces. DiMaggio and Sandler (1971) use a smooth intersection, but we consider this to be rather unrealistic (Vermeer, 1978, 1984). In recent years, there has been an increasing tendency to model plasticity by means of yield corners (or yield vertices). Examples thereof are the papers by Mandel (1965) and Rudnicki and Rice (1975).

The hardening-softening model employs seven constants, which is two more than the non-hardening model. The extra constants are ε^{f} and ε^{c}, the former is used in the $\phi^* - \bar{\varepsilon}^{p}$ relation (6.8) and the latter is used in the $c^* - \bar{\varepsilon}^{p}$ relation (7.2). ε^{f} is the strain needed to mobilise the limit friction angle, and ε^{c} denotes the strain that is needed to degrade the cohesion. The combination of friction hardening and cohesion softening seems very powerful, but a detailed study of reported test data is necessary for checking the relations to the effective strain as proposed in this study; slightly different relationships may turn out to be more appropriate.

In analogy with ϕ^* and c^*, we also introduced a relationship between the mobilised dilatancy angle ψ^* and the effective strain $\bar{\varepsilon}^{p}$. This relation derives from Rowe's stress dilatancy theory which has proved to be accurate for sand, but it is to some extent premature for cemented granular materials. Again, we need a follow-up by a detailed study of tests results. Attention should be focussed on the pre-peak hardening behaviour and not on the experimental results for the post-peak softening which are bound to be non-objective; specimens of different size give different post-peak responses due to non-uniformity of the strain over the specimen. Rudnicki and Rice (1975) analysed this non-uniformity for brittle rock, Vardoulakis (1980) did the same for sand, and Van Mier (1983) measured the non-uniformity on concrete specimens. In the next chapter we will show that the present model predicts non-uniform strain responses slightly prior and beyond peak.

8 Shear-band formation

For granular materials as well as for metals it is observed quite regularly that a smoothly varying deformation pattern suddenly changes and that all further deformations are localized in narrow so-called shear bands. This phenomenon is observed for instance during the collapse of embankments, dams, ground anchors (Fig. 8.1) and so on. The deformations in dense sand deposits and in rock formations are often completely dominated by these shear bands. A typical example is shown in Fig. 8.2, which gives the result of an experiment in a narrow vertical box filled with dense sand layers separated by thin layers of coloured sand. In the experiment, the flexible bottom has been pushed upwards to simulate a particular geological process. We see that the resulting deformation pattern is completely determined by a large number of shear bands.

In most soil mechanics literature a shear band is called a slip surface or a rupture surface. The traditional view is that a shear band forms an angle of $\theta = 45° + \frac{1}{2}\phi$ with the minor compressive stress. However, experiments by Arthur et al. (1977) and by

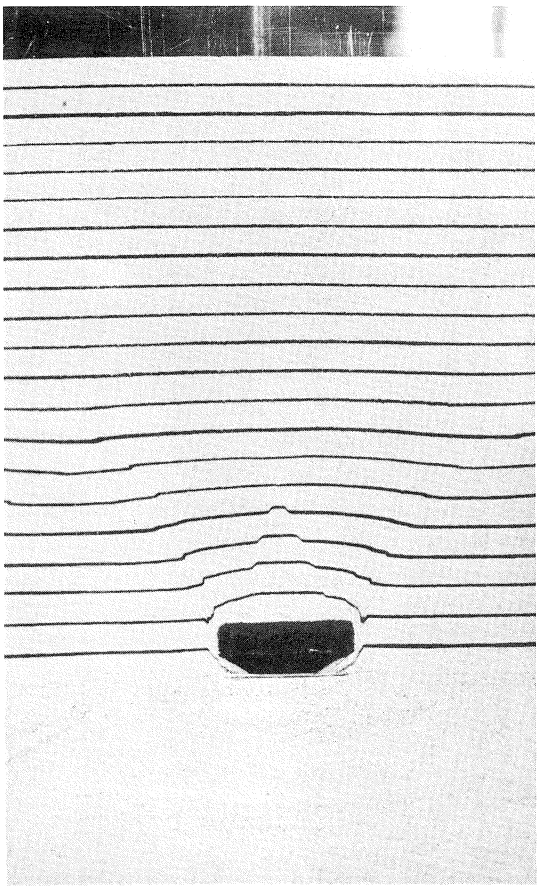

Fig. 8.1 Failure mechanism involving a shear band for a ground anchor.

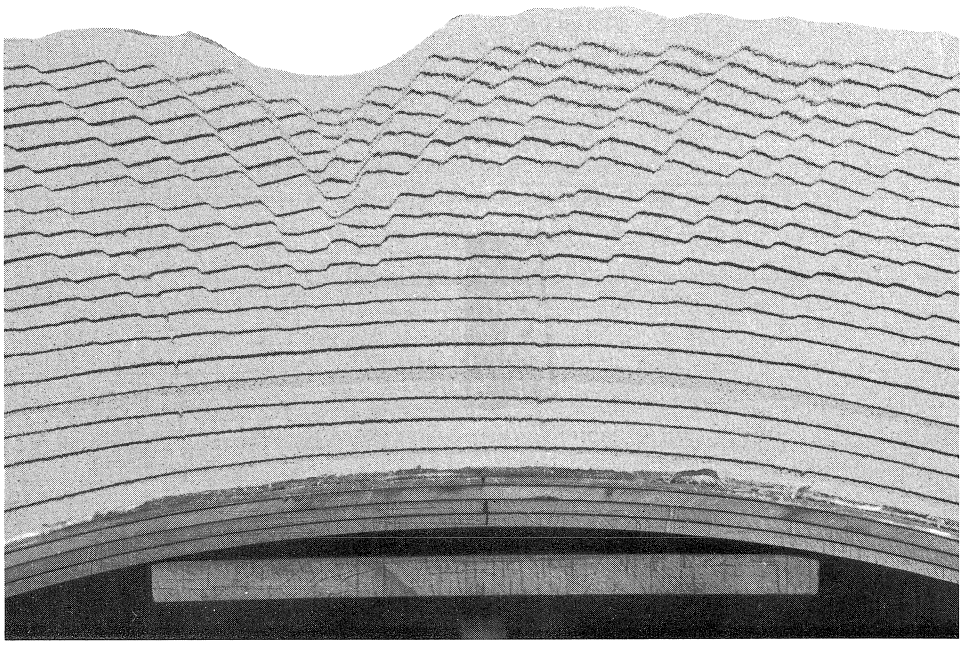

Fig. 8.2 Crestal faults over arch of uniform curvature, simulated in a sand box (Mandl, 1984).

Vardoulakis (1980) give a smaller inclination angle, namely $\theta = 45° + \frac{1}{4}(\phi + \psi)$. In the following, we will use the hardening-softening model to derive the experimental findings theoretically.

8.1 *Basic equations*

A shear band has a small, but finite thickness. In a sand body it has a thickness of about 20 times the mean grain size, which is equal to a few millimeters. In the following, we will again consider planar deformations, so that we have four stress and four strain components (see Section 4.1.). For the hardening-softening model elaborated in the preceding chapter, we have the following constitutive relation (see equation (7.6a)):

$$\dot{\boldsymbol{\varepsilon}} = \left\{ \mathbf{D}^{-1} + \frac{1}{h} \frac{\partial g}{\partial \boldsymbol{\sigma}} \frac{\partial f}{\partial \boldsymbol{\sigma}}^{\mathrm{T}} \right\} \dot{\boldsymbol{\sigma}} \tag{8.1}$$

with

$$\dot{\boldsymbol{\varepsilon}} = (\dot{\varepsilon}_{xx} \quad \dot{\varepsilon}_{yy} \quad \dot{\gamma}_{xy} \quad \dot{\varepsilon}_{zz})^{\mathrm{T}}$$

$$\dot{\boldsymbol{\sigma}} = (\dot{\sigma}_{xx} \quad \dot{\sigma}_{yy} \quad \dot{\sigma}_{xy} \quad \dot{\sigma}_{zz})^{\mathrm{T}}$$

Here, h is the hardening modulus and $\mathbf{D}^{-1}$ represents the elastic compliance matrix,

$$\mathbf{D}^{-1} = \frac{1}{E}\begin{bmatrix} 1 & -\nu & 0 & -\nu \\ -\nu & 1 & 0 & -\nu \\ 0 & 0 & 2(1-\nu) & 0 \\ -\nu & -\nu & 0 & 1 \end{bmatrix}$$

f is the yield function and g is the plastic potential function, for which we recall the definitions for the hardening-softening model

$$f = \tau^* - \sigma^* \sin \phi^* - c^*$$

$$g = \tau^* - \sigma^* \sin \psi^* + \text{constant}$$

In the sequel of this chapter we will need the first and the last of the four equations of the matrix equation (8.1). Therefore, we state these equations more fully:

$$\dot{\varepsilon}_{xx} = \left(\frac{1}{E} + \frac{1}{h}\frac{\partial g}{\partial \sigma_{xx}}\frac{\partial f}{\partial \sigma_{xx}}\right)\dot{\sigma}_{xx} + \left(\frac{-\nu}{E} + \frac{1}{h}\frac{\partial g}{\partial \sigma_{xx}}\frac{\partial f}{\partial \sigma_{yy}}\right)\dot{\sigma}_{yy} + \frac{1}{h}\frac{\partial g}{\partial \sigma_{xx}}\frac{\partial f}{\partial \sigma_{xy}}\dot{\sigma}_{xy} - \frac{\nu}{E}\dot{\sigma}_{zz}$$

$$\dot{\varepsilon}_{zz} = -\frac{\nu}{E}\dot{\sigma}_{xx} - \frac{\nu}{E}\dot{\sigma}_{yy} + \frac{1}{E}\dot{\sigma}_{zz} \tag{8.2}$$

where we have used the fact that σ_{zz} is the intermediate principal stress, so that $\partial f/\partial \sigma_{zz}$ and $\partial g/\partial \sigma_{zz}$ vanish.

We now consider a homogeneous element of granular material as shown in Fig. 8.3a.

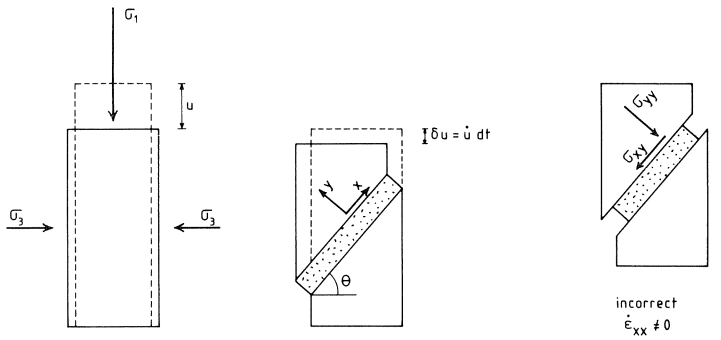

Fig. 8.3 a. Uniform deformation up to current state
b. Further deformation localized in a shear band
c. Incorrect mechanism.

The element may be a specimen that is loaded in a biaxial or a triaxial device. Up to some critical point, the deformations are quite homogeneous, giving stresses and strains which are uniform throughout the specimen. Beyond a critical point however, all further deformations are localized in a shear band as indicated in Fig. 8.3b, and the material outside the shear band is assumed to behave rigidly.

The shear band mechanism is subjected to some kinematical restrictions,

$$\dot{\varepsilon}_{xx} = 0 \qquad \dot{\varepsilon}_{zz} = 0 \tag{8.3}$$

which are caused by the fact that displacement jumps cannot occur (see Fig. 8.3c). The x-axis has conveniently been taken in the direction of the shear band.

In addition to the kinematical conditions, we have equilibrium conditions. Outside the shear band, the material does not deform any further, so that the stresses outside the band have to remain constant. Inside the shear band, there may be stress changes, but these changes cannot be arbitrary, as we must have equilibrium across the boundaries of the shear band. Hence, the stresses inside the shear band must satisfy.

$$\dot{\sigma}_{xy} = 0 \qquad \dot{\sigma}_{yy} = 0 \tag{8.4}$$

as we can have stress discontinuities only for the normal stresses σ_{xx} and σ_{zz} (Fig. 8.4).

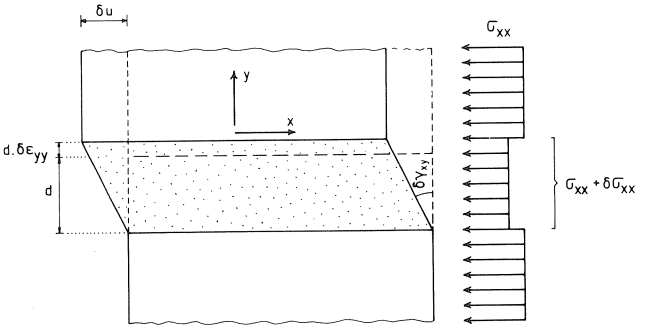

Fig. 8.4 Stress discontinuities across the shear-band boundaries.

8.2 *Elaboration of the equations*

Let us assume that the current state of the specimen is characterized by point C of the stress-strain curve in Fig. 8.5. Up to point C, the specimen deforms uniformly, but at point C we have a so-called bifurcation and a shear band develops. The critical value for the hardening modulus at which a shear band can first develop, and the inclination angle for a shear band, can be determined by inserting the constitutive equations (8.2) into the kinematic restrictions (8.3). Together with the equilibrium condition (8.4) this yields:

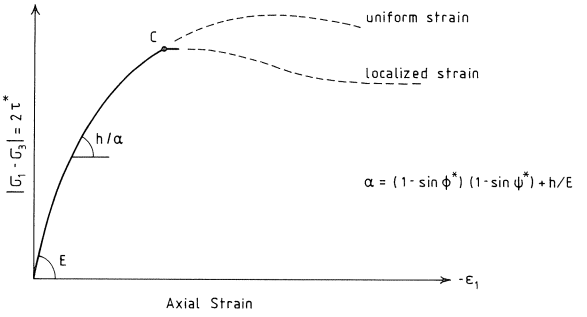

Fig. 8.5 Possible post-bifurcation response.

$$\dot{\varepsilon}_{xx} = \left(\frac{1}{E} + \frac{1}{h}\frac{\partial g}{\partial \sigma_{xx}}\frac{\partial f}{\partial \sigma_{xx}}\right)\dot{\sigma}_{xx} - \frac{\nu}{E}\dot{\sigma}_{zz} = 0$$

$$\dot{\varepsilon}_{zz} = -\frac{\nu}{E}\dot{\sigma}_{xx} + \frac{1}{E}\dot{\sigma}_{zz} = 0$$

Inserting the last equation into the first identity gives:

$$\dot{\varepsilon}_{xx} = \left\{\frac{1-\nu^2}{E} + \frac{1}{h}\frac{\partial g}{\partial \sigma_{xx}}\frac{\partial f}{\partial \sigma_{xx}}\right\}\dot{\sigma}_{xx} = 0$$

The particular case with $\dot{\sigma}_{xx} = 0$ is a trivial solution, which is of minor importance here. The other solutions are given by the shear-band equation

$$h = \frac{-E}{1-\nu^2}\frac{\partial g}{\partial \sigma_{xx}}\frac{\partial f}{\partial \sigma_{xx}} \tag{8.5}$$

The differentials is this equation can be evaluated by differentiating the functions f and g as given in the beginning of this chapter, yielding:

$$\frac{\partial f}{\partial \sigma_{xx}} = \tfrac{1}{2}\left(\frac{\sigma_{xx}-\sigma_{yy}}{2\tau^*} + \sin\phi^*\right) \qquad \frac{\partial g}{\partial \sigma_{xx}} = \tfrac{1}{2}\left(\frac{\sigma_{xx}-\sigma_{yy}}{2\tau^*} + \sin\psi^*\right)$$

The first terms in this equation relate to the inclination angle θ, as can be observed in Mohr's stress circle (Fig. 8.6). Hence, we can write:

$$\frac{\partial f}{\partial \sigma_{xx}} = \tfrac{1}{2}(\cos 2\theta + \sin\phi^*) \qquad \frac{\partial g}{\partial \sigma_{xx}} = \tfrac{1}{2}(\cos 2\theta + \sin\psi^*)$$

Substituting these expressions into equation (8.5), we obtain the relatively simple equation:

$$h = \frac{-E}{4(1-\nu^2)}(\cos 2\theta + \sin\psi^*)(\cos 2\theta + \sin\phi^*) \tag{8.6a}$$

or solving for $\cos 2\theta$,

$$\cos 2\theta = -\tfrac{1}{2}(\sin\phi^* + \sin\psi^*) \pm \tfrac{1}{2}\sqrt{(\sin\phi^* - \sin\psi^*)^2 - 16(1-\nu^2)h/E} \tag{8.6b}$$

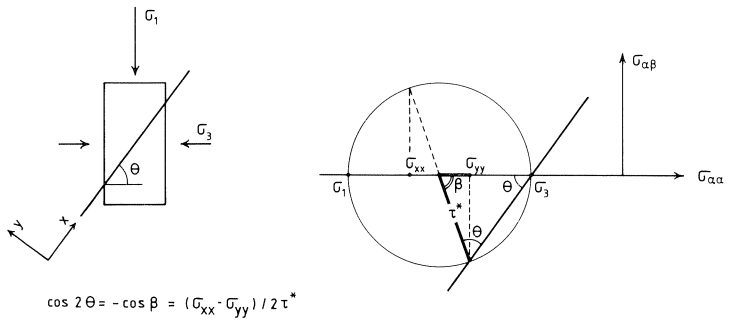

Fig. 8.6 Inclination angle and Mohr's stress circle.

Equation (8.6b) reveals that the inclination angle θ strongly depends on the current hardening modulus, which is represented in Fig. 8.7.

For large values of the hardening modulus h, that is in the beginning of loading, shear bands cannot develop, as this can take place only if equation (8.6b) has a real solution. The critical value of the hardening modulus h_c for which shear-band formation is first possible is derived from the condition that the expression under the square root has a non-negative sign, yielding:

$$h_c = \frac{E(\sin \phi^* - \sin \psi^*)^2}{16(1-\nu^2)} \tag{8.7}$$

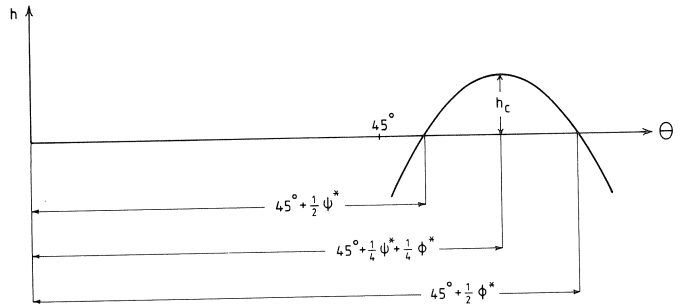

Fig. 8.7 Relation between hardening modulus and inclination angle of the shear band.

Then, that is for $h = h_c$, equation (8.6b) gives one unique solution for the inclination angle θ of the shear band

$$\cos 2\theta = -\tfrac{1}{2}(\sin \phi^* + \sin \psi^*) = -\sin (\tfrac{1}{2}\phi^* + \tfrac{1}{2}\psi^*) \cos (\tfrac{1}{2}\phi^* - \tfrac{1}{2}\psi^*)$$

or

$$\sin (90° - 2\theta) = -\sin (\tfrac{1}{2}\phi^* + \tfrac{1}{2}\psi^*) \cos (\tfrac{1}{2}\phi^* - \tfrac{1}{2}\psi^*)$$

This equation can further be simplified by noting that the difference between the mobilised friction angle and the mobilised dilatancy angle seldom exceeds 30°. Hence, $\cos (\frac{1}{2}\phi^* - \frac{1}{2}\psi^*)$ is in the range between 0.96 and 1.0. We can thus omit the cosine term in the above equation, so that we obtain for the inclination angle θ:

$$\theta \approx 45° + \tfrac{1}{4}(\phi^* + \psi^*) \quad \text{for} \quad h = h_c \tag{8.8}$$

which equals the experimental values given by Arthur et al. (1977), and by Vardoulakis (1980).

In many testing devices, the shear band mechanism of Fig. 8.3b cannot occur precisely because frictional end platens prevent a horizontal displacement of the material. Even a little friction at the end platens can delay the inception of a shear band. We then have a situation in which $h < h_c$, and we not longer have a unique inclination angle. Instead, two different inclination angles are now possible, as indicated by equation (8.6b)

and shown in Fig. 8.7. A special situation occurs for $h = 0$. Then equation (8.6b) gives the solutions:

$$\theta = 45° + \tfrac{1}{2}\psi^* \quad \text{or} \quad \theta = 45° + \tfrac{1}{2}\phi^* \quad \text{for} \quad h = 0 \tag{8.9}$$

Which solution will occur will depend on the particular boundary conditions and second order effects. It is noted that the solution for $\theta = 45° + \frac{1}{2}\psi^*$ corresponds to $\dot{\sigma}_{xx} = 0$.

We thus see that non-unique solutions (bifurcations) can occur if

$$h \leqslant \frac{E(\sin \phi^* - \sin \psi^*)^2}{16(1 - \nu^2)}$$

Hence, bifurcations are possible when the hardening modulus is still positive. The special case of associated plasticity ($\phi^* = \psi^*$) is an exception. Then non-unique solutions can occur only for $h \leqslant 0$, so that a shear band cannot develop in the hardening regime, but only at and beyond peak strength.

Finally, it is to be noted that the formation of shear bands can also be simulated in a numerical analysis. This is shown in Fig. 8.8.

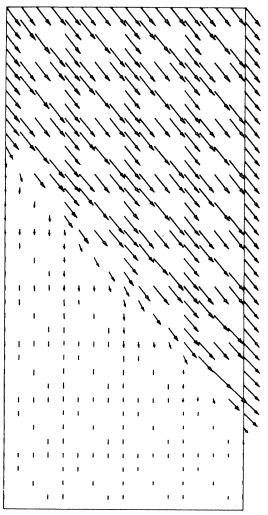

Fig. 8.8 Computed velocity field for a biaxial test (plane strain) involving a shear band.

8.3 *Previous studies*

Equation (8.7) for the critical hardening modulus was first derived by Mandel (1964). Mandel's paper is somewhat difficult to read and attracted relatively little notice. Moreover, he included inertia effects which complicated the analysis. Probably unaware of Mandel's paper, Rudnicki and Rice (1975) presented a similar analysis for rock. Their expression for the critical hardening modulus differs from equation (8.7), as they

used the Drucker-Prager yield criterion. Rudnicki and Rice also showed that a conventional small-strain formulation is accurate enough for a shear-band analysis, which justifies the present approach.

In 1980 Vardoulakis also used a Mohr-Coulomb type yield criterion, but his model is not entirely equivalent to the hardening-softening model developed here. Using a large velocity-gradient analysis, he derived a fairly complex condition for the critical hardening modulus, but arrived at the same simple equation (8.8) for the inclination angle of the shear band. Hence, the condition for the critical hardening modulus h_c was first derived by Mandel, and the expression for the inclination angle θ was first presented by Vardoulakis. The analysis given here, which gives both equations, was previously presented by Vermeer (1982). In contrast with Mandel, inertia effects have been omitted, while the difference from Vardoulakis' approach is the neglect of extra terms for large velocity gradients.

9 Plasticity models for cyclic loading

The development of reliable models for cyclic loading of materials is one of the most difficult tasks in constitutive modelling. At present, only models which aim at describing the cyclic behaviour of metals seem to be fairly successful. In this context we think of Besseling's fraction model (1958), Mróz's nested yield surface model (1967), and Dafalias' bounding surface model (1975). All these models are based on plasticity theory, although especially the last-mentioned model departs from classical concepts.

9.1 *Review of concepts*

For soils and concrete, the situation seems to be rather diffuse at the moment. Some attemps have been made to model cyclic soil behaviour using incrementally non-linear models (for instance Chambon and Darve, 1984, Robinet and Mohkam, 1982). In such models, the incremental stress-strain law takes the following form:

$$\dot{\boldsymbol{\sigma}} = \mathbf{D}(\boldsymbol{\sigma}, \dot{\boldsymbol{\sigma}}, \varkappa)\, \dot{\boldsymbol{\varepsilon}} \tag{9.1}$$

We see that the constitutive matrix now depends not only upon the current stress $\boldsymbol{\sigma}$ and some hardening parameter $\varkappa$, but also on the stress rate $\dot{\boldsymbol{\sigma}}$. Consequently, we have a non-linear relation between $\dot{\boldsymbol{\sigma}}$ and $\dot{\boldsymbol{\varepsilon}}$, which is not very convenient from a computational point of view. Further, we usually need a very large number of material constants (sometimes more than 20) in such models, which seems to preclude their use for practical engineering applications.

Another type of models which falls in this category of incrementally non-linear models is the endochronic theory, originally proposed by Valanis (1971) to describe metal behaviour, and extended by Bažant and Bhat (1976) for the description of granular materials. Indeed, some phenomena exhibited by metals and granular materials can be represented quite well using endochronic models. However, it appears that some other phenomena which should be captured in a good constitutive model describing the

hysteretic behaviour of granular and cemented granular materials can be represented only by applying artifices such as the concept of jump-kinematic hardening (Bažant, 1978). This, together with the fact that endochronic theories are incrementally non-linear, makes the use of this type of models rather unwieldy.

Yet another line of thinking was offered by Bažant and Kim (1979), who combined non-associated plasticity with the fracturing theory developed by Dougill (1976). In the latter theory, a criterion which is expressed in strains instead of in stresses is employed to bound the elastic domain. Further, fracturing theory deviates from plasticity theory in that unloading is assumed to occur along a secant branch instead of using the elastic stiffness (see Fig. 9.1). In its present stage of development, fracturing theory including the combination with plasticity does not seem to be of much practical significance, as some fundamental questions still have to be resolved. These partially relate to fracturing theory, as implementation in a computer program is hampered by some deficiencies in the theory. Further, the combination of plasticity and fracturing theory is not unique, and not all combinations lead to a theoretically consistent model.

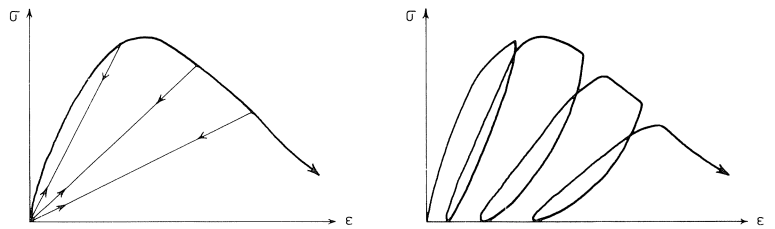

Fig. 9.1 Dougill's theory exaggerates the degradation of the unloading-reloading modulus.

Considering test results, we observe that near and beyond peak strength cemented granular materials indeed show an increasing degradation of the elastic stiffness due to micro-cracking. However, this effect is strongly exaggarated by Dougill's fracturing theory. In principle, this degradation can be incorporated in the theory of plasticity; rather than using a constant Young's modulus, it can be related to the porosity of the material. Instead of using the porosity directly, we can use a plastic deformation parameter such as the effective strain. Both elastic degradation and cohesive softening (see Chapter 7) are caused by micro-cracking of cemented materials and should be treated in a more or less similar way.

From this discussion it will be clear that there is little consensus as to which direction should be pursued in the constitutive modelling of the cyclic behaviour of granular and cemented granular materials. It is the authors' opinion that, pending other developments, it seems best to pursue ideas which have proved to be fairly successful in metal plasticity. Some attempts in this direction have already been published. Mróz (1978, 1979) and Dafalias (1979, 1982) have adapted their models for predicting the response of clay. Molenkamp (1982) has developed a kinematic hardening model for sand based upon Mróz's nested yield surface model. A bounding surface plasticity model which

describes cyclic behaviour of concrete has also been proposed (Fardis et al., 1983), although this particular model suffers from the drawback that it is also incrementally non-linear due to the fact that the elastic region is assumed to vanish.

In the following, we will first give an exposition of Dafalias' ideas. The treatment which will be given here, deviates from Dafalias' presentation in that our derivation follows the classical approach rather closely, whereas Dafalias' treatment uses the more mathematical concept of plastic internal variables. Next, we will discuss how hysteretic models for soils and concrete can be developed using these concepts, and the ideas developed in the preceding chapters for monotonic loading. Before proceeding, however, we note that Mróz's ideas are closely related to the work of Dafalias, and they can of course also be employed as a starting point for the development of models for describing the hysteretic behaviour of sand and concrete.

9.2 *Bounding surface plasticity*

We start our discussion from a typical stress-strain curve which may be obtained from a standard tension test on a metal, for instance on annealed copper (see Fig. 9.2a). If we subtract the elastic strain from the total strain (according to equation (3.1)), we get a stress-plastic strain diagram (Fig. 9.2b). The essence of bounding surface plasticity is that the current plastic modulus h is assumed to depend on the distance δ to the dashed line, the so-called bounding surface. So we assume the uniaxial relation

$$\dot{\sigma}_{11} = h\dot{\varepsilon}^{p}_{11} \tag{9.2}$$

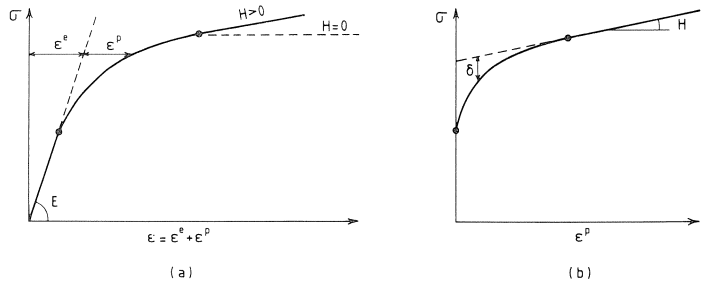

Fig. 9.2 The hardening modulus is calculated from the distance δ and the ultimate value H, which can be zero.

where the magnitude of h depends on the distance δ between the current stress σ_{11} and the bounding surface line, and possibly on some other parameters such as H, the slope of the bounding surface line. Hence we have

$$h = h(\delta, H, \text{other constants}) \tag{9.3}$$

The function h must obviously satisfy the requirements $h > H$, $\partial h/\partial\delta > 0$, $h = H$ for $\delta = 0$, and $h = \infty$ at the onset of yielding so that a smooth transition from elastic to elastic-plastic behaviour is obtained.

Generalizing to multi-dimensional stress space, we first revise the definition of a

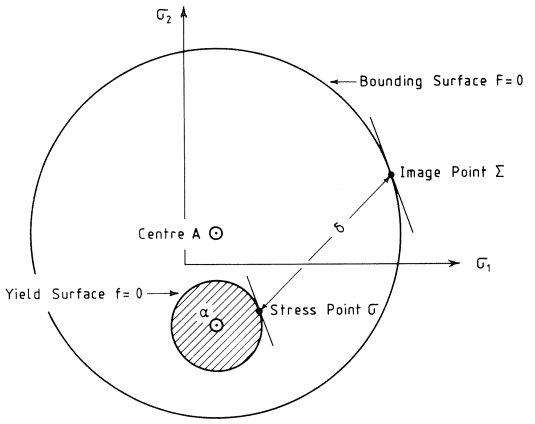

Fig. 9.3 Bounding surface around a relatively small elastic region.

yield function. When we introduced this concept for a non-hardening material (Chapter 4), the yield function f was assumed to depend only upon the stress tensor $\boldsymbol{\sigma}$, so that $f=f(\boldsymbol{\sigma})$. Extension to isotropic hardening forced us (Chapter 6) to include a hardening parameter in the definition for f; $f=f(\boldsymbol{\sigma}, \varkappa)$. For a proper description of cyclic loading it is necessary that the yield surface not only expands, but also translates (kinematic hardening, see Fig. 9.3). Hence, it is imperative that we include the current centre of the yield surface $\boldsymbol{\alpha}$ in our definition for f as well, so that a point is said to be in a plastic state whenever

$$f(\boldsymbol{\sigma}-\boldsymbol{\alpha}, \varkappa)=0 \tag{9.4}$$

In a similar way, we can extend the bounding surface line of Fig. 9.2b to a so-called bounding surface F in the multi-dimensional stress space, which always encompasses the yield surface f (see Fig. 9.3). The bounding surface is so defined that we also have $F=0$ if a point is in a plastic state. Obviously, the stress $\boldsymbol{\sigma}$ will never make F zero if the yield surface f lies inside the bounding surface F. Therefore, the function F is assumed to depend on an "image" stress tensor $\boldsymbol{\Sigma}$, so that

$$F=F(\boldsymbol{\Sigma}-\mathbf{A}, \varkappa) \tag{9.5}$$

where $\mathbf{A}$ is the centre of the bounding surface F. The question of how the stress $\boldsymbol{\Sigma}$ is obtained from the actual stress $\boldsymbol{\sigma}$ will be discussed in the next section.

As in the preceding chapters, the plastic strain rate is derived from a plastic potential g:

$$\dot{\boldsymbol{\varepsilon}}^{\mathrm{p}}=\lambda \frac{\partial g}{\partial \boldsymbol{\sigma}} \tag{9.6}$$

To determine the multiplier λ, we again make use of the consistency condition, which now reads:

$$\frac{\partial f}{\partial \boldsymbol{\sigma}}^{\mathrm{T}}(\dot{\boldsymbol{\sigma}}-\dot{\boldsymbol{\alpha}})+\lambda \frac{\partial f}{\partial \varkappa} \frac{\partial \varkappa}{\partial \boldsymbol{\varepsilon}^{\mathrm{p}}}^{\mathrm{T}} \frac{\partial g}{\partial \boldsymbol{\sigma}}=0 \tag{9.7}$$

Now, we must make an assumption as to the direction of $\dot{\boldsymbol{\alpha}}$. One of the most widely used assumptions is (Ziegler, 1959),

$$\dot{\boldsymbol{\alpha}} = \text{scalar} * (\boldsymbol{\sigma} - \boldsymbol{\alpha}) \tag{9.8}$$

with the subsidiary assumption that:

$$\text{scaler} * \frac{\partial f^{\mathrm{T}}}{\partial \boldsymbol{\sigma}} (\boldsymbol{\sigma} - \boldsymbol{\alpha}) = h^{\alpha} \frac{\partial f^{\mathrm{T}}}{\partial \boldsymbol{\sigma}} \dot{\boldsymbol{\varepsilon}}^{\mathrm{p}} \tag{9.9}$$

where h^{α} can be conceived as a plastic modulus for the centre of the yield surface. With aid of the flow rule we now obtain

$$\frac{\partial f^{\mathrm{T}}}{\partial \boldsymbol{\sigma}} \dot{\boldsymbol{\alpha}} = \lambda h^{\alpha} \frac{\partial f^{\mathrm{T}}}{\partial \boldsymbol{\sigma}} \frac{\partial g}{\partial \boldsymbol{\sigma}} \tag{9.10}$$

If we insert equations (9.9) and (9.10) in equation (9.6), we obtain the following expression for the plastic strain rate:

$$\dot{\boldsymbol{\varepsilon}}^{\mathrm{p}} = \frac{\dfrac{\partial f^{\mathrm{T}}}{\partial \boldsymbol{\sigma}} \dot{\boldsymbol{\sigma}}}{h^{\alpha} \dfrac{\partial f^{\mathrm{T}}}{\partial \boldsymbol{\sigma}} \dfrac{\partial g}{\partial \boldsymbol{\sigma}} - \dfrac{\partial f}{\partial \varkappa} \dfrac{\partial \varkappa^{\mathrm{T}}}{\partial \boldsymbol{\varepsilon}^{\mathrm{p}}} \dfrac{\partial g}{\partial \boldsymbol{\sigma}}} \frac{\partial g}{\partial \boldsymbol{\sigma}} \tag{9.11}$$

So far, the derivations closely resemble the classical concepts of kinematic/isotropic hardening. The salient difference between classical plasticity ideas and the bounding surface concept is that in the former approach we choose h, so that the total plastic stiffness due to isotropic and kinematic hardening follows from the choices for each of them. In the bounding surface concept, the total plastic stiffness is determined through the distance δ to the bounding surface, and the value of the modulus h^{α} follows as a result of the consistency condition. In the bounding surface philosophy we replace equation (9.11) by:

$$\dot{\boldsymbol{\varepsilon}}^{\mathrm{p}} = \frac{\dfrac{\partial f^{\mathrm{T}}}{\partial \boldsymbol{\sigma}} \dot{\boldsymbol{\sigma}}}{h \dfrac{\partial f^{\mathrm{T}}}{\partial \boldsymbol{\sigma}} \dfrac{\partial g}{\partial \boldsymbol{\sigma}}} \frac{\partial g}{\partial \boldsymbol{\sigma}} \tag{9.12}$$

It can now be deduced that this equation reduces to equation (9.2) for the uniaxial case. Comparing equations (9.11) and (9.12), we see that h^{α} is given by

$$h^{\alpha} = h + \frac{\dfrac{\partial f}{\partial \varkappa} \dfrac{\partial \varkappa^{\mathrm{T}}}{\partial \boldsymbol{\varepsilon}^{\mathrm{p}}} \dfrac{\partial g}{\partial \boldsymbol{\sigma}}}{\dfrac{\partial f^{\mathrm{T}}}{\partial \boldsymbol{\sigma}} \dfrac{\partial g}{\partial \boldsymbol{\sigma}}} \tag{9.13}$$

Hence, in classical plasticity, we choose h^α and $\partial f/\partial \varkappa$ and the plastic modulus h will result from those choices, whereas in the bounding surface approach we take h and $\partial f/\partial \varkappa$ as starting point and derive h^α from the consistency condition.

9.3 *The image stress* $\boldsymbol{\Sigma}$

In the preceding section the image stress $\boldsymbol{\Sigma}$ was introduced. This image stress tensor was assumed to be on the bounding surface F whenever the actual stress $\boldsymbol{\sigma}$ was on the yield surface f. This condition is of course not sufficient to define $\boldsymbol{\Sigma}$, but is merely a requirement. Another requirement is imposed on $\boldsymbol{\Sigma}$ by the condition that the bounding surface and the yield surface may only touch, bur never intersect. This implies that in the limiting state ($\boldsymbol{\sigma} = \boldsymbol{\Sigma}$) we must require (see Fig. 9.4a),

$$\frac{\partial f}{\partial \boldsymbol{\sigma}} = \frac{\partial F}{\partial \boldsymbol{\sigma}} \tag{9.14}$$

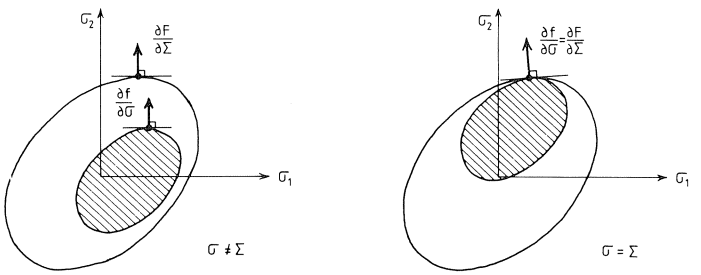

Fig. 9.4 The elastic region translates within the bounding surface.

This condition is satisfied a priori if it is required that $\boldsymbol{\Sigma}$ is so defined that $\boldsymbol{\sigma}$ and $\boldsymbol{\Sigma}$ have the same normals respectively to the yield surface and to the bounding surface during the entire loading process (Dafalias and Popov, 1976, see Fig. 9.4b),

$$\frac{\partial f}{\partial \boldsymbol{\sigma}} = \frac{\partial F}{\partial \boldsymbol{\Sigma}} \tag{9.15}$$

For strictly convex yield surfaces and bounding surfaces this relation defines a unique image stress tensor for any given stress which is on the yield surface. As we will argue in the next section, this idea is not very suitable for frictional materials. For metals however, it is rather convenient. Moreover, it allows for a more general kinematic hardening rule than given by equations (9.9) and (9.10), see Dafalias and Popov (1976).

With a definition for the image stress tensor the constitutive model is almost completed. We only have to define some rule for the translation of the centre of the bounding surface, as represented by the vector **A**. Here, it is important to recall the requirement that the bounding and the yield surface may only touch, but not intersect. This requirement can be satisfied by defining:

$$\dot{\mathbf{A}} = \dot{\boldsymbol{\alpha}} - \text{scalar} * (\boldsymbol{\Sigma} - \boldsymbol{\sigma}) \tag{9.16}$$

where the scalar may be determined from the consistency condition for the bounding surface: $\dot{F}(\Sigma - \mathrm{A}, \varkappa) = 0$.

9.4 *Specialization to frictional materials*

For frictional materials, proposition (9.15) for determining the image stress is not very convenient, at least if we adhere to the concept of friction hardening. Then the normal to any point of the yield surface can never correspond to the normal of any point of the bounding surface (see Fig. 9.5a). For this reason another mapping, namely

$$\Sigma = \sigma + b\mathbb{D}\frac{\partial f}{\partial \sigma} \tag{9.16}$$

is suggested, where b is a scalar multiplier which may be determined from the condition that Σ be on the bounding surface: $F(\Sigma - \mathrm{A}, \varkappa) = 0$. This mapping cannot be used for arbitrary yield and bounding surfaces, as it is not guaranteed a priori that they will not intersect. For judicious choices of the yield and bounding surfaces, however, this condition can definitely be satisfied. An example thereof is the pure friction hardening model for dry sand (see Chapter 6), which obeys the Mohr-Coulomb failure criterion. This criterion is now written as

$$f = \tau^* - \sigma^*(\sin\phi^* + \sin\alpha) \tag{9.17}$$

where ϕ^* is the mobilised friction angle, and α is the inclination of the centreline of the yield surface (see Fig. 9.5b). The bounding surface is now postulated to be of the form

$$F = T^* - \Sigma^* \sin\phi \tag{9.18}$$

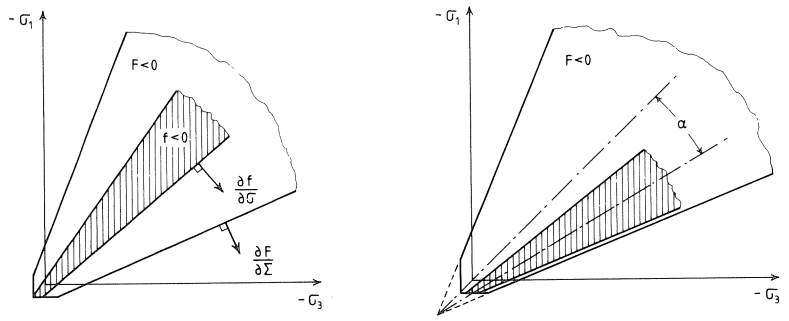

Fig. 9.5 Proposed bounding surface and elastic region.

where T^* and Σ^* are functions of the image stress tensor Σ, and are defined in analogy with to σ^* and τ^*. It is recalled that ϕ is the friction angle in the limiting state. It is noted that kinematic hardening on the bounding surface as discussed in the preceding section is neglected in equation (9.18). This is certainly not correct, as the movement of the bounding surface is coupled to the movement of the yield surface through the condition that both surfaces may not intersect. For triaxial testing conditions with $\sigma_2 = \sigma_3$, how-

ever, neglecting the kinematic hardening on the bounding surface does not lead to intersecting yield and bounding surfaces, at least for the Mohr-Coulomb function.

The model which is defined by equations (9.16) to (9.18) satisfies condition (9.14). To show this, we first note that for yield surfaces, which are linear in the principal stresses (see equation 4.18), a Taylor's expansion yields for the multiplier b:

$$b = -\frac{F(\boldsymbol{\sigma})}{\frac{\partial F^{\mathrm{T}}}{\partial \boldsymbol{\sigma}} \mathbf{D} \frac{\partial f}{\partial \boldsymbol{\sigma}}} \tag{9.19}$$

Hence we have upon loading:

$$\boldsymbol{\Sigma} = \boldsymbol{\sigma} - \frac{F(\boldsymbol{\sigma})}{\frac{\partial F^{\mathrm{T}}}{\partial \boldsymbol{\sigma}} \mathbf{D} \frac{\partial f}{\partial \boldsymbol{\sigma}}} \mathbf{D} \frac{\partial f}{\partial \boldsymbol{\sigma}} \tag{9.20}$$

When the stress $\boldsymbol{\sigma}$ is on the bounding surface, we have by definition $F(\boldsymbol{\sigma}) = 0$, so that according to equation (9.20), the image stress coincides with the actual stress: $\boldsymbol{\sigma} = \boldsymbol{\Sigma}$. Furthermore, we can derive from equations (9.16) and (9.17) that

$$\frac{\partial f}{\partial \boldsymbol{\sigma}} = \frac{\partial \tau^*}{\partial \boldsymbol{\sigma}} - (\sin \phi^* + \sin \alpha) \frac{\partial \sigma^*}{\partial \boldsymbol{\sigma}} \tag{9.21}$$

$$\frac{\partial F}{\partial \boldsymbol{\Sigma}} = \frac{\partial T^*}{\partial \boldsymbol{\Sigma}} - \sin \phi \frac{\partial \Sigma^*}{\partial \boldsymbol{\Sigma}} \tag{9.22}$$

In the limiting state it follows from $\boldsymbol{\sigma} = \boldsymbol{\Sigma}$ that $\tau^* = T^*$ and $\sigma^* = \Sigma^*$, and hence

$$\frac{\partial \tau^*}{\partial \boldsymbol{\sigma}} = \frac{\partial T^*}{\partial \boldsymbol{\Sigma}} \tag{9.23}$$

$$\frac{\partial \sigma^*}{\partial \boldsymbol{\sigma}} = \frac{\partial \Sigma^*}{\partial \boldsymbol{\Sigma}} \tag{9.24}$$

so that we can rewrite equation (9.22) as follows

$$\frac{\partial F}{\partial \boldsymbol{\Sigma}} = \frac{\partial F}{\partial \boldsymbol{\sigma}} = \frac{\partial \tau^*}{\partial \boldsymbol{\sigma}} - \sin \phi \frac{\partial \sigma^*}{\partial \boldsymbol{\sigma}} \tag{9.25}$$

Comparing equations (9.21) and (9.25), we observe that the requirement (9.14) is complied with, provided that in the limiting state we have

$$\sin \phi = \sin \phi^* + \sin \alpha \tag{9.26}$$

In order to get an idea of the merits of this type of models, it is useful to consider an example of a sand specimen subjected to cyclic loading in a triaxial device. Here we have considered a sand with the same properties as in Chapter 5. It is assumed that the specimen was first loaded isotropically and subsequently subjected to a number of axial loading cycles. The response of the specimen according to the model as outlined above

is shown in Fig. 9.6. In the calculations the following functional relationship for the plastic modulus h has been used:

$$h = a(\delta^0)^b \frac{\delta}{\delta - \delta^0} \tag{9.27}$$

where a and b are parameters which may be used to fit test data adequately. δ^0 is the distance between the actual stress $\boldsymbol{\sigma}$ and the image stress $\boldsymbol{\Sigma}$ at the beginning of each loading process.

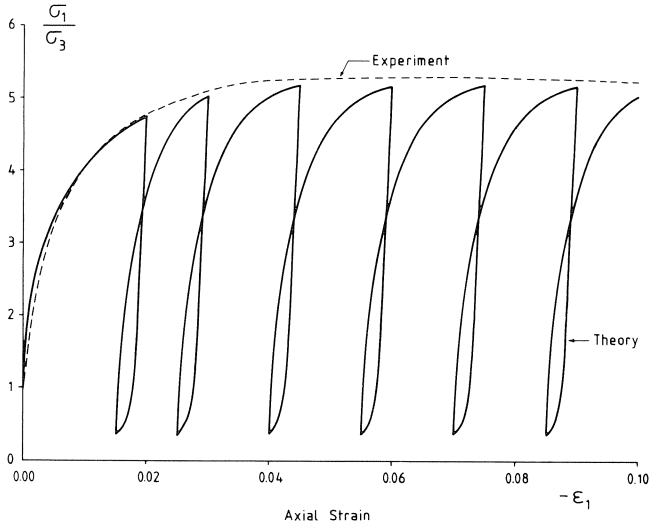

Fig. 9.6 Model simulation of cyclic loading of dry sand in a triaxial apparatus.

10 Conclusions

Considering test results, we observe that concrete and rock are stiffer and stronger than a loose granular material, but that plastic yielding is described reasonably well by a Mohr-Coulomb yield criterion which involves a friction angle and a cohesive strength. Plastic yielding is nearly always accompanied by a plastic volume increase, but the amount of dilation differs considerably from the value that would follow from associated plasticity theory.

The soil mechanics concept of a dilatancy angle is useful for concrete and rock as well. Slightly before and beyond peak strength the dilatancy angle attains a constant value depending on the particular material. The dilatancy angle is at least 20° less than the friction angle. Because of this large difference we are forced to use a non-associated flow rule. This flow rule corresponds to a plastic potential which resembles the yield function, but which involves a dilatancy angle instead of a friction angle.

The need for non-associated plasticity has been demonstrated by numerical results

for some practical problems. The use of an associated flow rule leads to an overestimation of the stiffness and the load-carrying capacity. The most striking numerical result is the occurrence of post-peak softening as a consequence entirely of the non-associated flow rule. This can be explained from the violation of Drucker's stability postulate.

We have described three material models of increasing complexity. The first is a perfectly-plastic model. It might be referred to as a "student's model" as it is a good introduction to plasticity theory. This five-parameter model is appropriate for limit analyses and for a gross approximation of deformations under working loads. The perfectly-plastic model has been extended to obtain a model with friction hardening and cohesion softening. This model could be called an "engineer's model", as it strikes a balance between accuracy and simplicity. When extending the second model to include phenomena such as hysteresis and strain-accumulation in cyclic loading, the complexity again increases, and we arrive at a "scientist's model". Nevertheless, a computationally attractive model can be established when using the concept of a bounding surface and a mapping rule. In order to employ these concepts within a non-associated model of the Mohr-Coulomb type, we have proposed a new mapping rule.

A general feature of this study is the unified treatment of the mechanical behaviour of sand, rock, and concrete. The difference between soil mechanics, concrete mechanics and rock mechanics basically lies in the application. Then the three disciplines diverge because of the dominant role of water in soils, the role of fissures and joints in rocks and the role of tension cracks and reinforcement in concrete.

11 Acknowledgement

The second author's contributions to Chapter 9 were assisted by financial support from CUR-Committee A 26 "Concrete Mechanics".

12 Principal notation

c cohesion
c^* mobilised cohesion
E Young's modulus
ν Poisson's ratio
ϕ angle of internal friction
ϕ^* mobilised angle of internal friction
ψ dilatancy angle
ψ^* mobilised dilatancy angle
τ^* radius of Mohr's circle
σ^* centre of Mohr's stress circle
f yield function
g plastic potential function
h hardening modulus

13 References

ALLERSMA, H. G. B. (1982), Photo-elastic stress analysis in simple shear, Proc. IUTAM Conf. on Deformation and Failure of Granular Materials, Delft, 345-353. Balkema, Rotterdam.

ARTHUR. J. R. F., T. DUNSTAN, Q. A. J. AL-ANI and A. ASSADI (1977), Plastic deformation and failure in granular media, Géotechnique 27, 53-74.

BAŽANT, Z. P. and P. BHAT (1976), Endochronic theory of inelasticity and failure of concrete, J. Eng. Mech. Div. ASCE 102, No. EM4, 701-722.

BAŽANT, Z. P. (1978), Endochronic inelasticity and incremental plasticity, Int. J. Solids and Structures 14, 691-714.

BAŽANT, Z. P. and S. S. KIM (1979), Plastic-fracturing theory for concrete, J. Eng. Mech. Div. ASCE 105, No. EM3, 407-428.

BESSELING, J. F. (1958), A theory of elastic, plastic and creep deformations of an initially isotropic material, J. Appl. Mech. 25, 529-536.

BORST, R. DE (1982a), Calculation of collapse loads using higher order elements, Proc. IUTAM Conf. on Deformation and Failure of Granular Materials, Delft, 503-513. Balkema, Rotterdam.

BORST, R. DE (1982b), Numerical prediction of the ultimate bearing capacity of soil masses, Report No. 220 of the Geotechnical Laboratory, Delft University of Technology, Delft.

BORST, R. DE and P. A. VERMEER (1984), Possibilities and limitations of finite elements for limit analysis, Géotechnique 34, No. 2, 199-210.

CHAMBON, R. and F. DARVE (1984), On two directionally linearizable incremental constitutive laws. In: Constitutive relations for Soils (Eds. G. Gudehus, F. Darve and I. Vardoulakis), Balkema, Rotterdam.

CHEN, W. F. (1982), Plasticity in reinforced concrete. McGraw-Hill.

COULOMB, C. A. (1776), Essai sur une application des règles de maximis et minimis a quelques problèmes de statique rélatifs a l'architecture, Mémoires de l'Academie Royale des Sciences 7, 343-382.

COX, A. D., G. EASON and H. G. HOPKINS (1961), Axially symmetric plastic deformation in soils, Phil. Trans. Roy. Soc. 254, No. 1, 1-47.

CHRISTENSEN, J. and K. WILLAM (1983), Finite element analysis of concrete in shear, Proc. Symp. on the Interaction of Non-nuclear Munitions with Structures, U.S. Air Force Academy, Colorado, 101-106.

DAFALIAS, Y. F. and E. P. POPOV (1975), A model of nonlinearly hardening materials, Acta Mechanica 21, 173-192.

DAFALIAS, Y. F. and E. P. POPOV (1976), Plastic internal variables formalism of cyclic plasticity, ASME J. Appl. Mech. 98, 645-650.

DAFALIAS, Y. F. (1979), A model of soil behaviour under monotonic and cyclic loading conditions, Transactions 5th Int. Conf. on Structural Mech. in Reactor Technology, Berlin, K 1/8. North-Holland Publ. Co.

DAFALIAS, Y. F. and L. R. HERRMANN (1982), Bounding surface formulation of soil plasticity. In: Soil Mechanics - Transient and Cyclic Loads, 10: 253-282. John Wiley and Sons, Chichester.

DAVIS, E. H. (1968), Theories of plasticity and the failure of soil masses. In: Soil Mechanics, Selected Topics (Ed. I. K. Lee), 341-380, Butterworths, London.

DIMAGGIO, F. L. and I. S. SANDLER (1971), Material models for granular soils, J. Eng. Mech. Division ASCE 97, No. EM3, 935-950.

DOUGILL, J. W. (1976), On stable progressively fracturing solids, J. Applied Math. Physics (ZAMP) 27, 423-437.

DRUCKER, D. C. and W. PRAGER (1952), Soil mechanics and plastic analysis or limit design, Q. Applied Math. 10, No. 2, 157-165.

DRUCKER, D. C. (1964), Concept of path independence and material stability for soils, Proc. IUTAM Symp. on Rheology and Soil Mech., Grenoble, pp. 24-45. Springer Verlag, Berlin, 1966.

FARDIS, M. N., B. ALIBE and J. L. TASSOULAS (1983), Monotonic and cyclic constitutive law for concrete, J. Eng. Mech. Div. ASCE 109, No. 2, 516-536.

GERSTLE, K. H. et al. (1978), Strength of concrete under multiaxial stress states, Proc. Douglas-McHenry Int. Symp. on Concrete and Concrete structures, ACI Specialty Publication SP-55, 103-131.
GOLDSCHEIDER, M. (1984), True triaxial tests on dense sands. In: Constitutive relations for Soils (Eds. G. Gudehus, F. Darve and I. Vardoulakis), Balkema, Rotterdam.
GREEN, S. J. and S. R. SWANSON (1973), Static constitutive relations for concrete, AFWL-TR-72-244, Air Force Weapons Laboratory, Kirtland Air Force Base, New Mexico.
HANSEN, J. BRINCH (1965), Some stress-strain relationships for soils, Proc. 6th Int. Conf. Soil Mech. Found. Engng, Montreal, Vol. 1, 231-234.
HANSEN, C. E. BENT (1958), Line ruptures regarded as narrow rupture zones - Basic equations based on kinematic considerations, Proc. Brussels Conf. 58 on Earth Pressure Problems, Vol. 1, 39-48.
HETTLER, A. and I. VARDOULAKIS (1984), Behaviour of dry sand tested in a large triaxial apparatus, Géotechnique 34, No. 2, 183-198.
JOSSELIN DE JONG, G. DE (1971), The double sliding free rotating model for granular assemblies, Géotechnique 21, 155-163.
KOITER, W. T. (1960), General theorems for elastic-plastic solids. In: Progress in Solid Mechanics, Vol. 1 (Eds. Sneddon and Hill), 165-221. North-Holland Publishing Co., Amsterdam.
KOVARI, K. (1977), The elasto-plastic analysis in the design practice of underground openings. In: Finite Elements in Geomechanics (Ed. G. Gudehus), 413-478. Wiley, London.
LADE, P. V. and J. M. DUNCAN (1975), Elastoplastic stress-strain theory for cohesionless soil, J. Geot. Engng Div. ASCE 101, 1034-1053.
LADE, P. V. (1983), Three-parameter failure criterion for concrete, J. Eng. Mech. Div. ASCE 108, No. 5, 850-863.
MANDEL, J. (1964), Conditions de stabilité et postulat de Drucker, Proc. IUTAM Symp. on Rheology and Soil Mechanics, Grenoble, 331-341. Springer Verlag, Berlin, 1966.
MANDEL J. (1965), Généralisation de la théorie de plasticité de W. T. Koiter, Int. J. Solids Structures 1, 273-295.
MANDL, G. (1984), Private Communication.
MATSUOKA, H. and T. NAKAI (1982), A new failure criterion for soils in three-dimensional stresses, Proc. IUTAM Conf. on Deformation and Failure of Granular Materials, Delft, 253-263. Balkema, Rotterdam.
MIER, J. G. M. VAN (1984), Complete stress-strain behaviour and damaging status of concrete under multiaxial conditions, Proc. RILEM/CEB Symp. on Concrete under Multiaxial Conditions, Toulouse, 75-85.
MICHELIS, P. N. (1981), Work-softening and hardening behaviour of granular rocks, Rock Mechanics 14, 187-200.
MOLENKAMP, F. (1982), Kinematic model for alternating loading - ALTERNAT, Report CO-218596/7, Delft Soil Mechanics Laboratory, Delft, The Netherlands.
MRÓZ, Z. (1967), On the description of anisotropic workhardening, J. Mech. Phys. Solids 15, 163-175.
MRÓZ, Z., V. A. NORRIS and O. C. ZIENKIEWICZ, (1978), An anisotropic hardening model for soils and its application to cyclic loading, Int. J. Numer. Anal. Meth. Geom. 2, No. 3, 203-221.
MRÓZ, Z., V. A. NORRIS and O. C. ZIENKIEWICZ (1979), Application of an anisotropic hardening model in the analysis of elasto-plastic deformation of soil, Géotechnique 29, No. 1, 1-34.
NAYAK, G. C. and O. C. ZIENKIEWICZ (1972), Elasto-plastic stress analysis. A generalisation for various constitutive relations including strain softening, Int. J. Num. Meth. Engng 5, 113-135.
NEWMAN, J. B. (1979), Concrete under complex stress. In: Developments in Concrete Technology (Ed. F. T. Lyon). Butterworth, London.
RADENKOVIC, D. (1961), Théorèmes limites pour un matériau de Coulomb à dilatation non standardisée, C.R.Ac.Sc. 252, Paris, 4103-4104.
REYNOLDS, O. (1885), On the dilatancy of media composed of rigid particles in contact, Phil. Mag. 5th Ser. 20, pp. 469.
ROBINET, J. C. and M. MOHKAM (1982). A non-linear constitutive law for sands. Proc. IUTAM Conf. on Deformation and Failure of granular Materials, Delft, 313-322. Balkema, Rotterdam.

ROSCOE, K. H. (1953), An apparatus for the application of simple shear to soil samples, Proc. 3rd Int. Conf. Soil Mech., Zurich, Vol. 1, 129-170.
ROSCOE, K. H. (1970), Tenth Rankine Lecture: The influence of strains in soil mechanics, Géotechnique 20, No. 2, 129-170.
ROSCOE, K. N., A. N. SCHOFIELD and A. THURAIRAJAH (1963), Yielding of clays in states wetter than critical, Géotechnique 13, No. 3, 211-240.
ROWE, P. W. (1971), Theoretical meaning and observed values of deformation parameters for soil, Proc. Roscoe Memorial Symp. on Stress-Strain Behaviour of Soils, Cambridge, 143-194. Foulis, Henley-on-Thames, 1972.
RUDNICKI, J. W. and J. R. RICE (1975), Conditions of the localization of the deformation in pressure-sensitive materials, J. Mech. Phys. Solids 23, 371-394.
SALENÇON, J. (1977), Applications of the Theory of Plasticity in Soil Mechanics. John Wiley & Sons, Chichester.
SCHOFIELD, A. N. and C. P. WROTH (1968), Critical State Soil Mechanics. McGraw-Hill, London.
SCHREYER, H. L. (1983), A third-invariant plasticity theory for frictional materials J. Struct. Mech. 11, No. 2, 177-196.
SCHREYER, H. L. and S. M. BABCOCK (1984), A third-invariant plasticity theory for low-strength concrete, submitted for publication.
SMITH, I. M. (1982), Programming the Finite Element Method with application to geomechanics. John Wiley & Sons, Chichester.
STROUD, M. A. (1971), The behaviour of sand at low stress levels in the simple-shear apparatus. Ph.D. Thesis, Cambridge University.
STURE, S. (1983), Experimental modeling of strength and deformation behavior of concrete in direct shear, Proc. Symp. on the Interaction of Non-nuclear Munitions with Structures, U.S. Air Force Academy, Colorado, 95-100.
TATSUOKA, F. and K. ISHIHARA (1975), Undrained deformation and liquefaction of sand under cylic stresses, Soils and Foundations 15, No. 1, 29-44.
TRAINA, L. A. (1983), Experimental stress-strain behaviour of a low strength concrete under multiaxial states of stress, AFWL-TR-82-92, Air Force Weapons Laboratory, Kirtland Air Force Base, New Mexico.
TRESCA, H. (1868), Mémoire sur l'écoulement des corps solides, Mém. pres. par div. Savants 18, 733-799.
VALANIS, K. C. (1971), A theory of viscoplasticity without a yield surface, Arch. of Mech. 23, 517-535.
VARDOULAKIS, I. (1980), Shear band inclination and shear modulus of sand in biaxial tests, Int. J. Numer. Anal. Meth. Geomech. 4, No. 2, 103-119.
VERMEER, P. A. (1978), A double hardening model for sand, Géotechnique 28, No. 4, 413-433.
VERMEER, P. A. (1980), Formulation and analysis of sand deformation problems, Dissertation, Delft Univ. of Technology, Delft.
VERMEER, P. A. (1981), A formulation and analysis of granular flow, Proc. Int. Symp. Mech. Behavior of Structured Media, Ottawa, Part B, 325-339. Elsevier, Amsterdam.
VERMEER, P. A. (1982), A simple shear-band analysis using compliances, Proc. IUTAM Conf. on Deformation and Failure of Granular Materials, Delft, 493-499. Balkema, Rotterdam.
VERMEER, P. A. (1984), A five-constant model unifying well-established concepts. In: Constitutive Relations for Soils (Eds. G. Gudehus et al., 175-197, Balkema, Rotterdam.
VERMEER, P. A. and W. SUTJIADI (1985), The uplift resistance of shallow embedded anchors, Proc. 11th Int. Conf. Soil Mech. Engng, San Francisco. In press by Balkema, Rotterdam.
WILLAM, K. J. and E. P. WARNKE (1974), Constitutive model for the triaxial behaviour of concrete, Colloquium on "Concrete structures subjected to triaxial stresses", ISMES Bergamo, IABSE Report Vol. 19.
WOOD, D. M. and M. BUDHU (1980), The behaviour of Leighton Buzzard Sand in cyclic simple shear tests, Proc. Int. Symp. on Soils under Cyclic and Transient Loading, Swansea, Vol. 1, 9-21. Balkema, Rotterdam.
ZAADNOORDIJK, W. J. (1983), Cone resistance at the surface of a sand bed, Graduation study at the Geotechnical Laboratory, Delft University of Technology, Delft, The Netherlands.
ZIEGLER, H. A. (1959), A modification of Prager's hardening rule, Quart. Appl. Mech. 17, 55-65.
ZIENKIEWICZ, O. C., C. HUMPHESON and R. W. LEWIS (1975), Associated and non-associated visco-plasticity and plasticity in soil mechanics, Géotechnique 25, No. 4, 671-689.